Available on the CERN CDS information server **CMS PAS TRK-10-001**

CMS Physics Analysis Summary

Contact: cms-pog-conveners-tracking@cern.ch 2010/04/08

Tracking and Vertexing Results from First Collisions

The CMS Collaboration

Abstract

CMS recorded the first LHC collisions at center of mass energies of 900 GeV and 2.36 TeV in December 2009. We reconstruct the trajectories of charged particles produced in the collisions using the all-silicon tracker and measure their momenta in the 3.8 T solenoidal magnetic field. We have assessed the performance of track reconstruction in the data and compared it to the expectation from simulation.

1 Introduction

The reconstructed tracks of charged particles are among the most fundamental objects in the reconstruction of pp collisions. Tracks can be used to reconstruct the decays of hadrons, photon conversions, and nuclear interactions. In addition, tracks are components of the reconstruction of other objects such as electrons, muons, taus, and b-quark jets.

CMS recorded the first collisions from the LHC in December 2009 at energies of $\sqrt{s} = 900\,\text{GeV}$ and 2.36 TeV. We have studied the reconstructed tracks in this data to commission the tracking detectors and to reconstruct basic physics objects as a demonstration of the performance. In this analysis summary we first describe the underlying qualities of the reconstructed tracks. A fundamental measurement from tracking is the reconstruction of the position of the colliding beams, and we present results from two methods. We then use the tracks to reconstruct the decays of K^0_S, Λ, ϕ, $\Xi^{\pm}$, and $K^{\star}(892)$. For the K^0_S and Λ, we also measure the lifetime. The measurement of the masses and lifetimes of these well-known particles provides an initial validation of the reconstruction (for both prompt and displaced tracks), vertexing, and the magnetic field. As a first investigation of the tracker material, we use the tracks to reconstruct photon conversions and nuclear interactions. Finally, we present an initial study of b-tagging observables.

2 Track Reconstruction

The default track reconstruction at CMS is performed by the combinatorial track finder (CTF) [1]. Triplets of hits in the tracker or pairs of hits with an additional constraint from the beamspot or a vertex are used as initial estimates, or seeds, of tracks. The seeds are then propagated outward in a search for compatible hits. As hits are found, they are added to the seed trajectory and the track parameters and uncertainties are updated. This search continues until either the limit of the tracker is reached or no more compatible hits can be found, yielding the collection of hits that belong to the track. In the final step, this collection of hits is fit to obtain the best estimate of the track parameters.

The CTF performs multiple iterations. Between each iteration, hits that can be unambiguously assigned to tracks in the previous iteration are removed from the collection of tracker hits to create a smaller collection that can be used in the subsequent iteration. At the end of each iteration, the reconstructed tracks are filtered to remove tracks that are likely fake and to flag the expected purity of the tracks.

3 Data and Simulated Samples and Event Selection

The results presented in this analysis summary have been obtained using the data collected by the CMS experiment in the runs with colliding beams at the center-of-mass energies of 900 GeV and 2.36 TeV, the solenoid magnetic field at the nominal value of 3.8 T and the silicon pixel and the silicon strip tracker detectors enabled and with the nominal high voltage bias applied to the sensors.

Due to the relatively low LHC luminosity the CMS readout was triggered by the beam scintillator counter (BSC) trigger to collect minimum-bias collision events and by the beam pick-up timing detector to detect the passage of the beam bunches [2]. Events have been selected where the time coincidence between the signals of the two arms of the BSC ($3.23 < |\eta| < 4.65$) is compatible with particles from a pp collision and incompatible with beam-produced particles which cross the detector from one end to the other. The number of selected events is

about 305 000. Most of the analyses presented in this summary reduce the background from non-collision events further and select useful events for tracking studies by requiring events to have: (a) one primary vertex reconstructed with at least four tracks; (b) the reconstructed position along the beam line within ± 15 cm of the nominal CMS detector center, and (c) the distance in the transverse plane from the nominal beam line within 2 cm; and (d) a fraction of *highPurity* tracks (see Sect. 4) larger than 20% if the number of reconstructed tracks is larger than 10. After this further selection about 260 000 events are left.

For the the data set used for the results of this analysis summary the alignment parameters of the silicon tracker were computed with about two million of cosmic ray tracks collected in November 2009 and the nominal values of the alignment parameter errors have been used in the track reconstruction. Since the applied procedure was similar to the one discussed in Ref. [3], the resulting precision is also very similar.

The simulated events used in this summary are minimum-bias events produced with the PYTHIA 6.4 [4] event generator, tune D6T [5], at center-of-mass energies of 900 GeV and 2.36 TeV (about 10 M events each) and processed with a simulation of the CMS detector response based on GEANT 4 [6]. The misalignment, miscalibrations and dead channel map corresponding to the detector status and calibration accuracy at the time of the first LHC collisions have been included in the simulation. The longitudinal distribution of the primary collision vertices has been tuned to match the real data.

4 Basic Tracking Distributions

Before using the tracks in further reconstruction of resonances or other objects, we make a comparison of basic distributions between the data and simulation. During reconstruction tracks are separated in categories of expected purity based on a series of cuts on the normalized χ^2, the longitudinal and transverse impact parameters, and their significances. Tracks failing the loosest selection are rejected, while those that pass the tightest selection are labeled *highPurity*. Further details on the *highPurity* selection can be found in Appendix A. We select tracks that pass the *highPurity* selection, then apply further cleanup by requiring the significance of the longitudinal impact parameter $|d_z/\sigma| < 10$ (where σ includes the uncertainties on d_z and the primary vertex) and $\sigma_{p_T}/p_T < 10\%$. Figure 1 shows a comparison of data and simulation for the following distributions: number of tracks per event; number of hits used per track; transverse momentum, p_T; pseudorapidity, η; azimuthal angle, ϕ; transverse impact parameter, d_{xy}, with respect to the primary vertex; longitudinal impact parameter, d_z, with respect to the primary vertex; and normalized χ^2.

The distribution of the number of tracks per event has been normalized to the number of events. Other distributions have been normalized to the number of reconstructed tracks in the data. The asymmetry of the ϕ distribution is due to inactive modules.

5 Reconstruction of Primary Vertices

The reconstruction of the primary interaction vertex in the event starts from the track collection. Prompt tracks are selected based on the transverse impact parameter, number of hits, and the normalized track χ^2. The selected tracks are then clustered in z and the cluster is fit with an adaptive vertex fit [7], where tracks in the vertex are assigned a weight between 0 and 1 based on their compatibility with the common vertex.

Figure 2 shows the primary vertex distributions separately in x, y, and z from a single run.

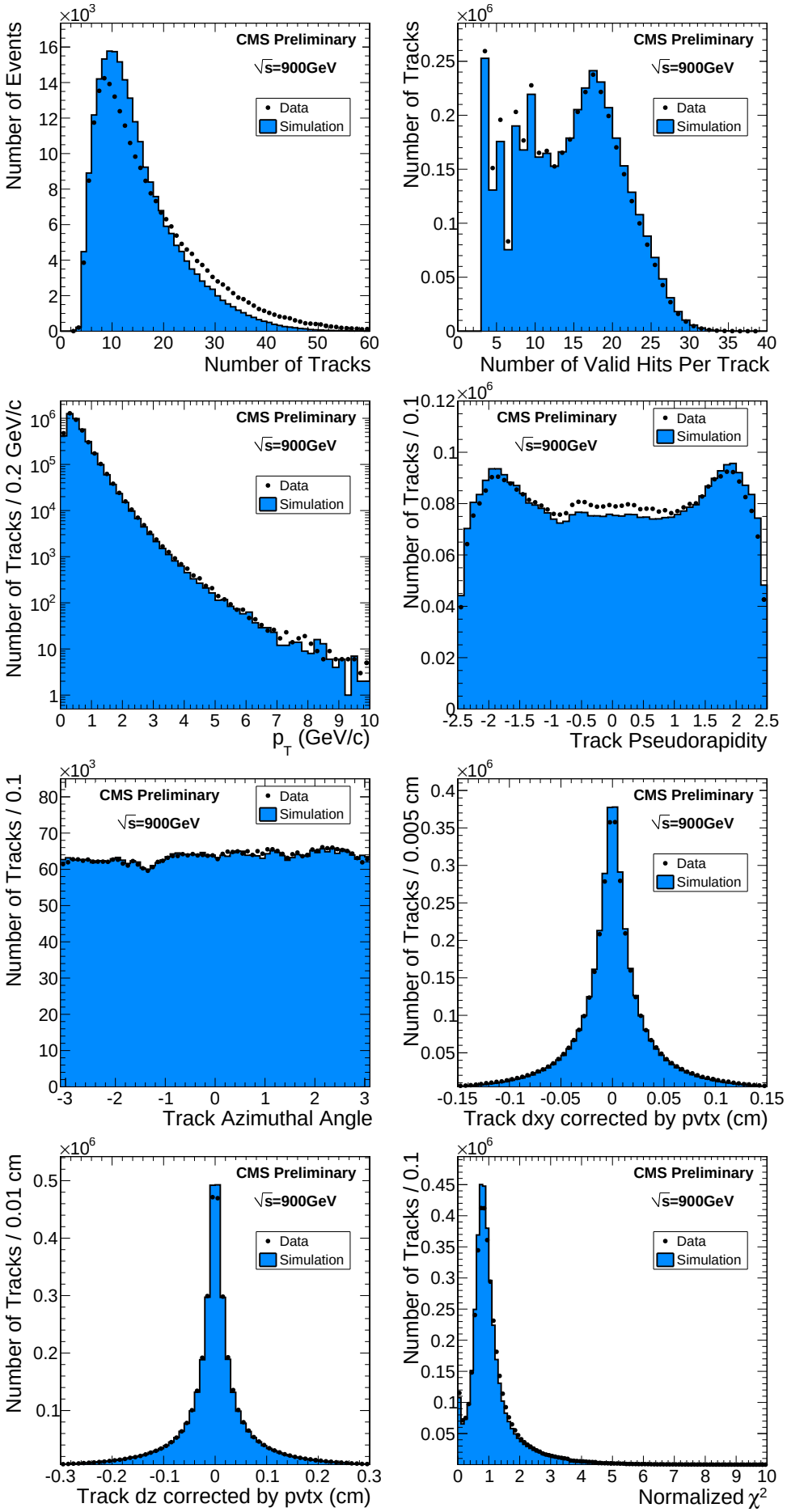

Figure 1: Comparison of data (points) and simulation (blue histogram) tracking distributions.

The width of the primary vertex distribution is dominated by the beam width and results are shown on the figure. The overall shape of the luminous region can be seen further in Fig. 3 where the primary vertex distributions are shown in two dimensions.

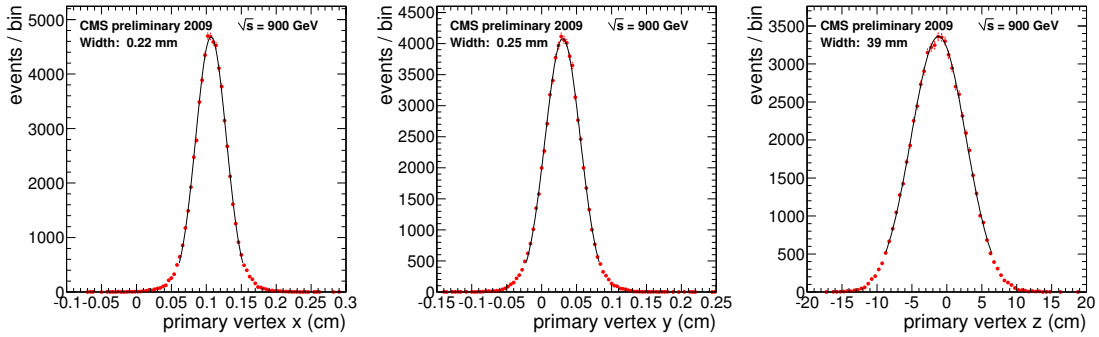

Figure 2: Primary vertex distributions from a single run.

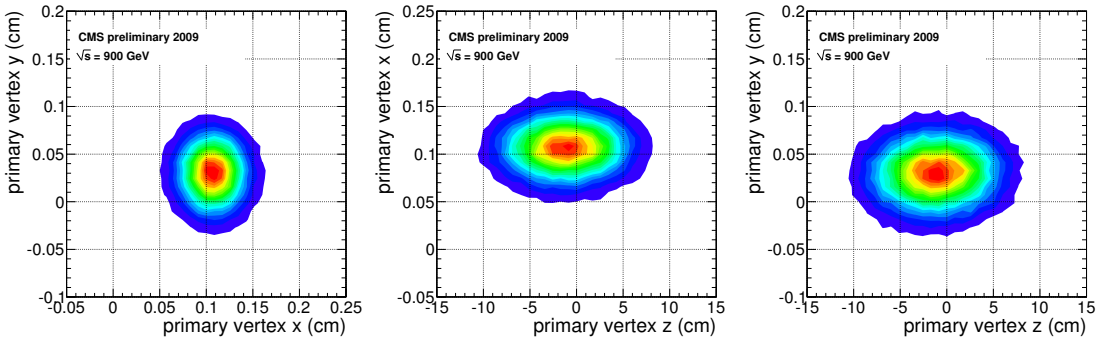

Figure 3: 2D plots of the primary vertex distributions from a single run.

The primary vertex resolution is a strong function of the number of tracks used in fitting the vertex and the p_T of those tracks. To measure the resolution as a function of the number of tracks in the vertex, the tracks in an event are split into two different sets and used to independently fit the primary vertex. The distribution of the difference in the fitted vertex positions can then be used to extract the resolution.

Figure 4 shows the measured primary vertex resolution as a function of the number of tracks in x (left), y (middle), and z (right). Results are shown for both the December data and the simulation and a good agreement in the curves is seen. The difference between the measured vertex positions, divided by the sum in quadrature of the uncertainties reported by the fit, is referred to as the *pull*. Figure 5 shows the measured pulls on the primary vertex. The pulls are roughly flat and close to unity.

To examine the effect of the sum of the transverse momenta of the tracks in the vertex, we can study the resolution vs. the number of tracks in the vertex for different average p_T of tracks in the vertex. Figure 6 shows the resolution for different average p_T in x, y, and z. The corresponding pulls are shown in Fig. 7. Even though our resolution differs for the different p_T regions shown, the simulation is able to track the data fairly well.

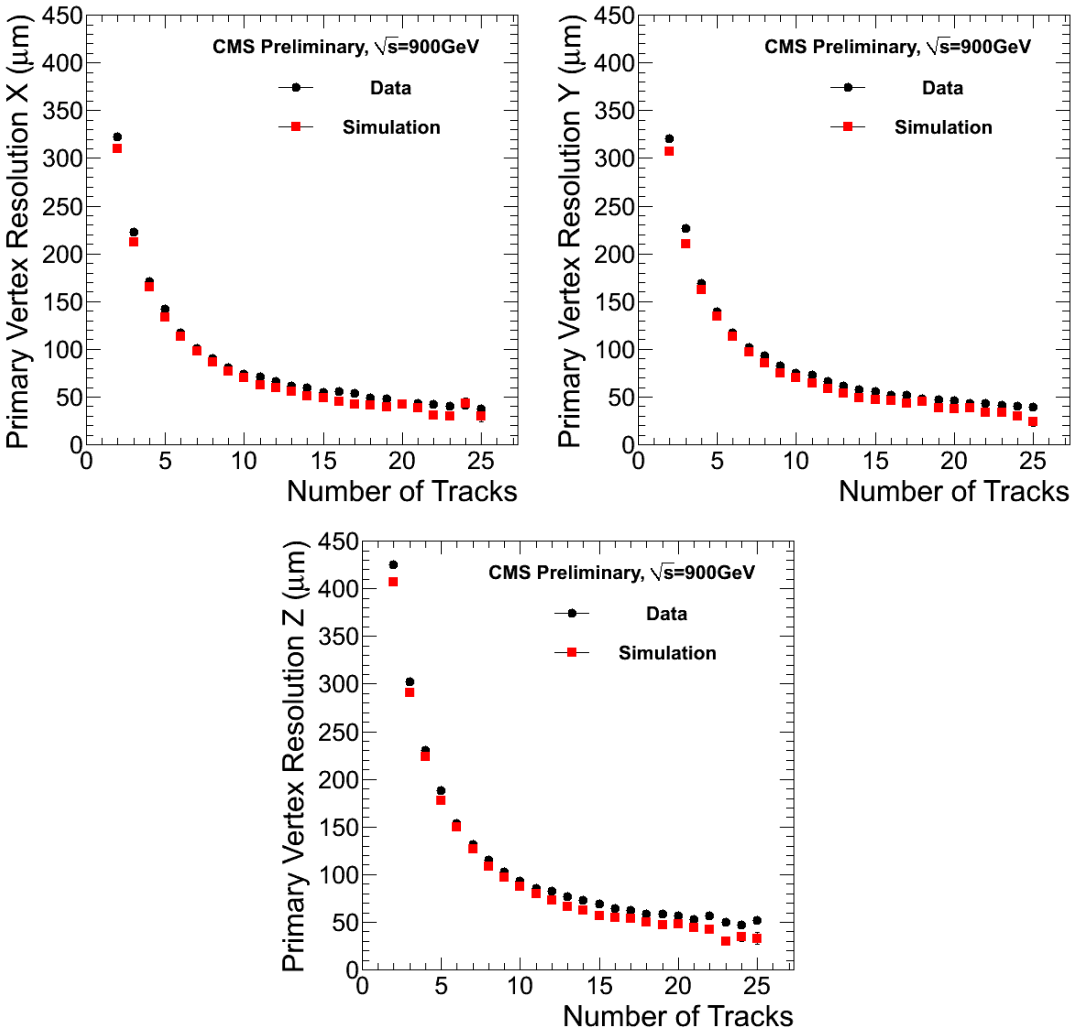

Figure 4: Primary vertex resolution as a function of the number of tracks used in the fitted vertex.

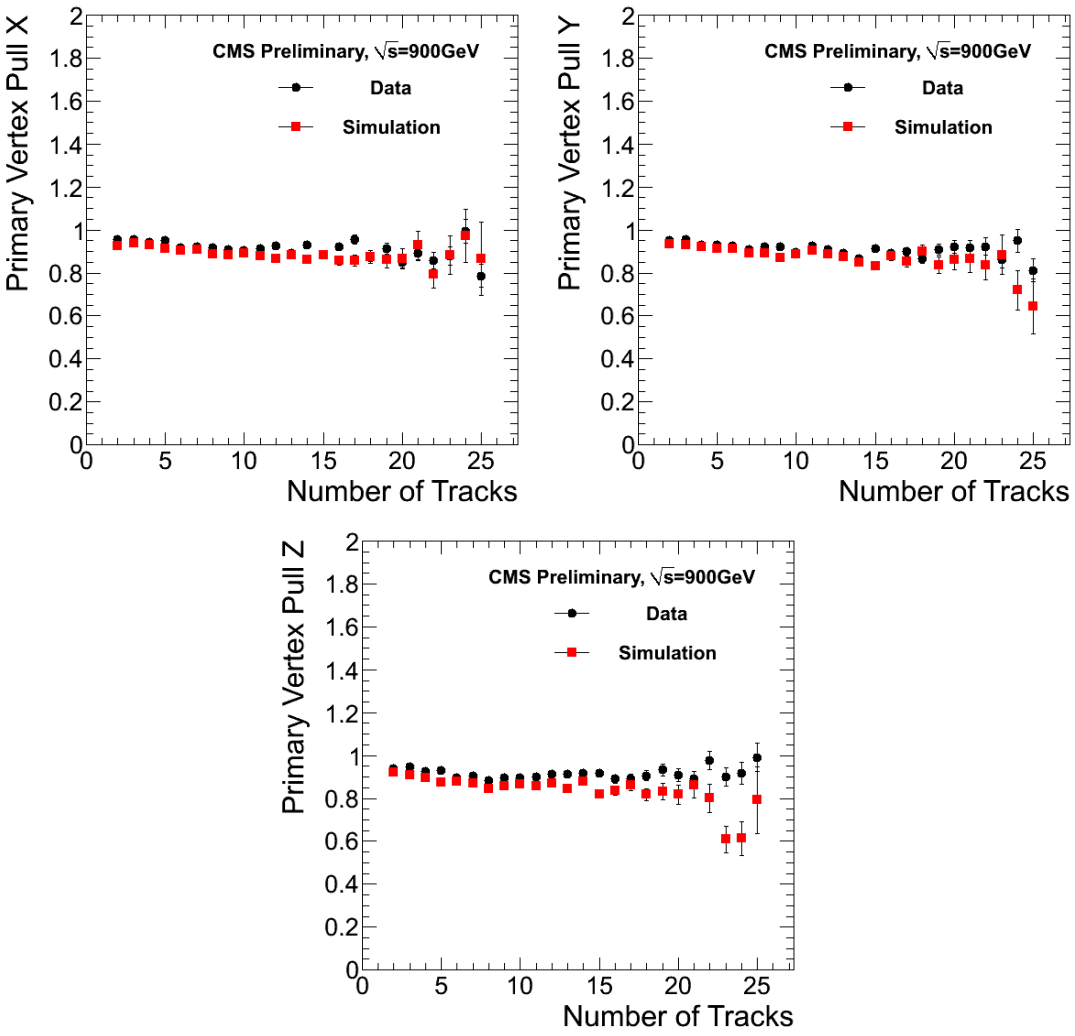

Figure 5: Fitted pulls from the primary vertex distributions.

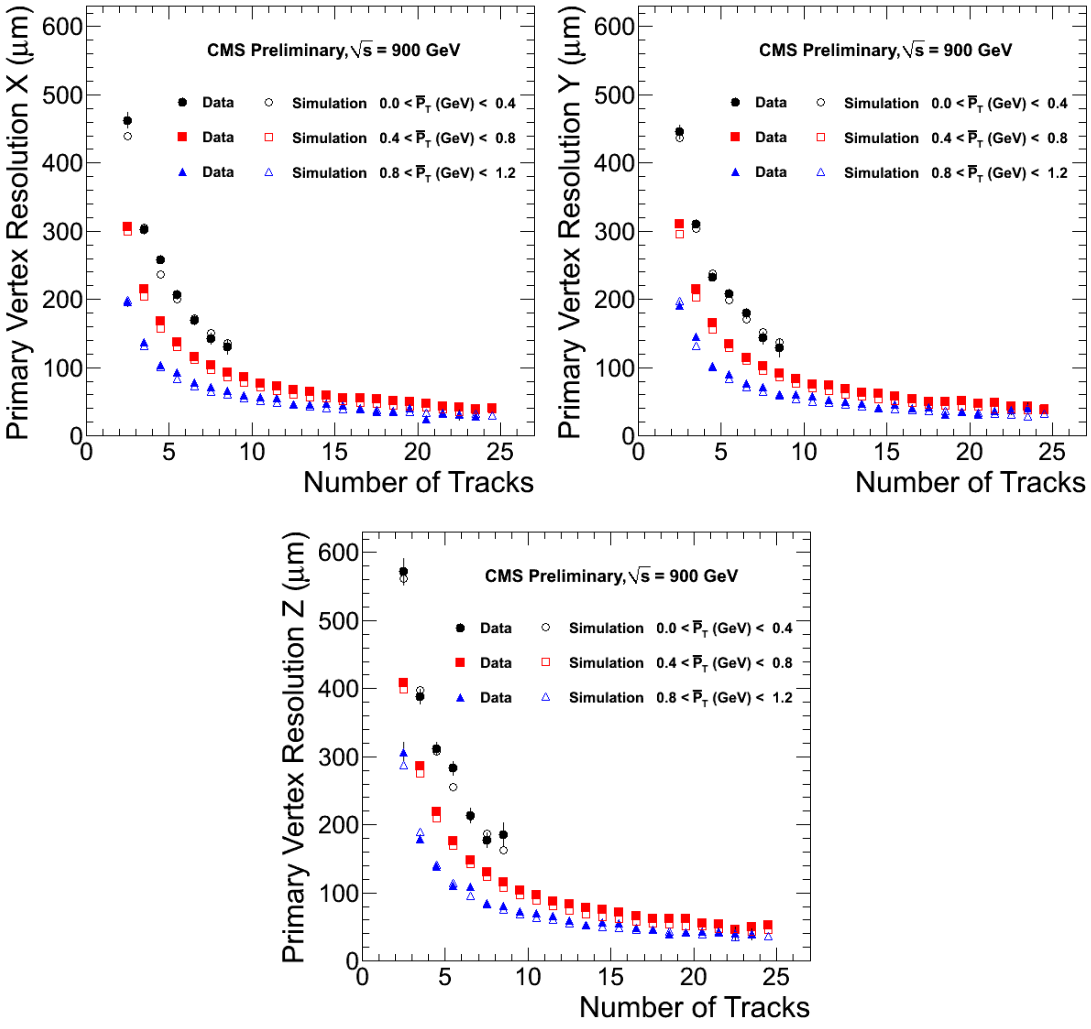

Figure 6: Resolution vs. number of tracks for different average p_{T}.

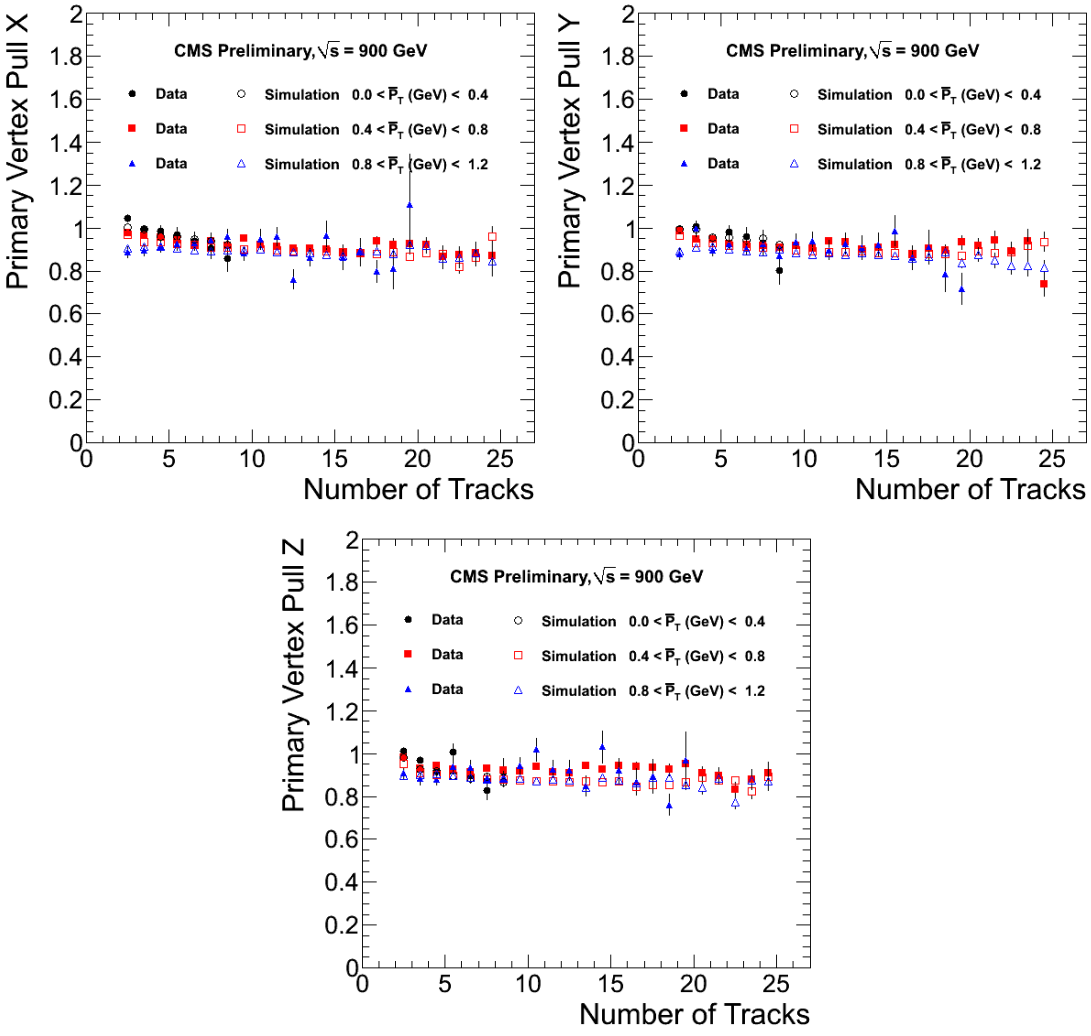

Figure 7: Fitted pulls vs. number of tracks for different average p_{T}.

6 Reconstruction of the LHC Beamspot

The beamspot represents the profile of the luminous region where the LHC beams collide at CMS. The beamspot is determined in an average over many events, in contrast to the event-by-event primary vertex which gives the precise position of a single collision. A precise measurement of the position and slope of the beamspot is an important component of the event reconstruction. The beam position can be used, especially in the High Level Trigger, as a precise estimate of the primary interaction point prior to the reconstruction of the primary vertex and even as the primary interaction point in low multiplicity data.

When the beamspot is displaced from the expected position, there is a correlation between the transverse impact parameter (d_{xy}) and the angle of a track at the point of closest approach (ϕ_0). To first order the d_{xy} for tracks coming from the primary vertex can be parametrized by

$$d_{xy}(\phi_0, z) = x_0 \cdot \sin\phi_0 + \frac{dx}{dz} \cdot \sin\phi_0 \cdot z - y_0 \cdot \cos\phi_0 - \frac{dy}{dz} \cdot \cos\phi_0 \cdot z, \tag{1}$$

where x_0 and y_0 are the position of the beam at $z = 0$, and $\frac{dx}{dz}$ and $\frac{dy}{dz}$ are the x and y slopes of the beam. The beamspot fit [8] uses an iterative χ^2 fit to exploit this correlation between d_{xy} and ϕ_0, looping over a sample of reconstructed tracks to determine the parameters of the beam.

The left plot of Fig. 8 shows the $d_{xy} - \phi_0$ correlation for a displaced beamspot when $(0, 0)$ is assumed for the beamspot in a single run, with the results of the beamspot fit overlaid. The right plot of Fig. 8 shows the same correlation using the fitted beamspot.

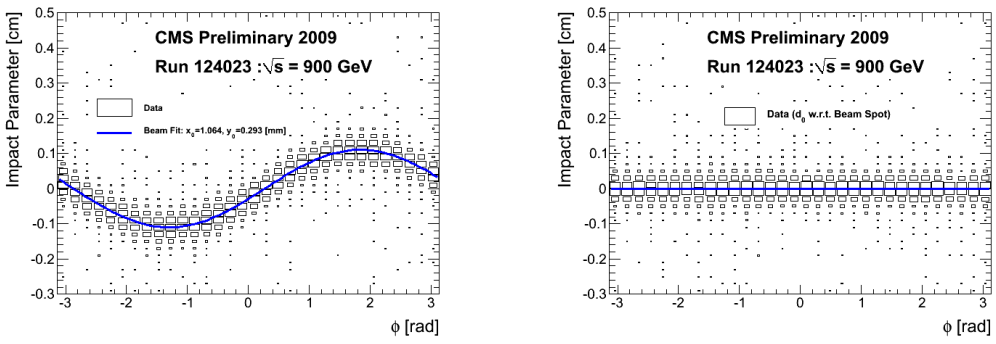

Figure 8: Plots of d_{xy} vs. ϕ_0 for reconstructed tracks in a single run, using (0,0) as the beamspot position (left) and using the fitted beamspot (right).

During the 2009 data-taking, a beamspot was fit during every LHC fill. The position of reconstructed primary vertices can also be used to determine the beam position. The x, y, and z positions of the primary vertex are fit to 1-D gaussian distributions, assuming the absence of a substantial slope in the beam. (The slopes were also determined in the beamspot fit and found to be on the order of 0.1 mrad.) Figure 9 shows a comparison of the fitted x_0, y_0, and z_0 values obtained from the primary vertex fit and the beamspot fit. The statistical uncertainty on the gaussian fit is slightly smaller than the uncertainty from the beamspot fit, but the values are in good agreement with each other.

In addition to the (x, y, z) position of the center of the beam, the width of the beam in the transverse plane (σ_x and σ_y) and the length in z (σ_z) can be obtained from both the primary vertex

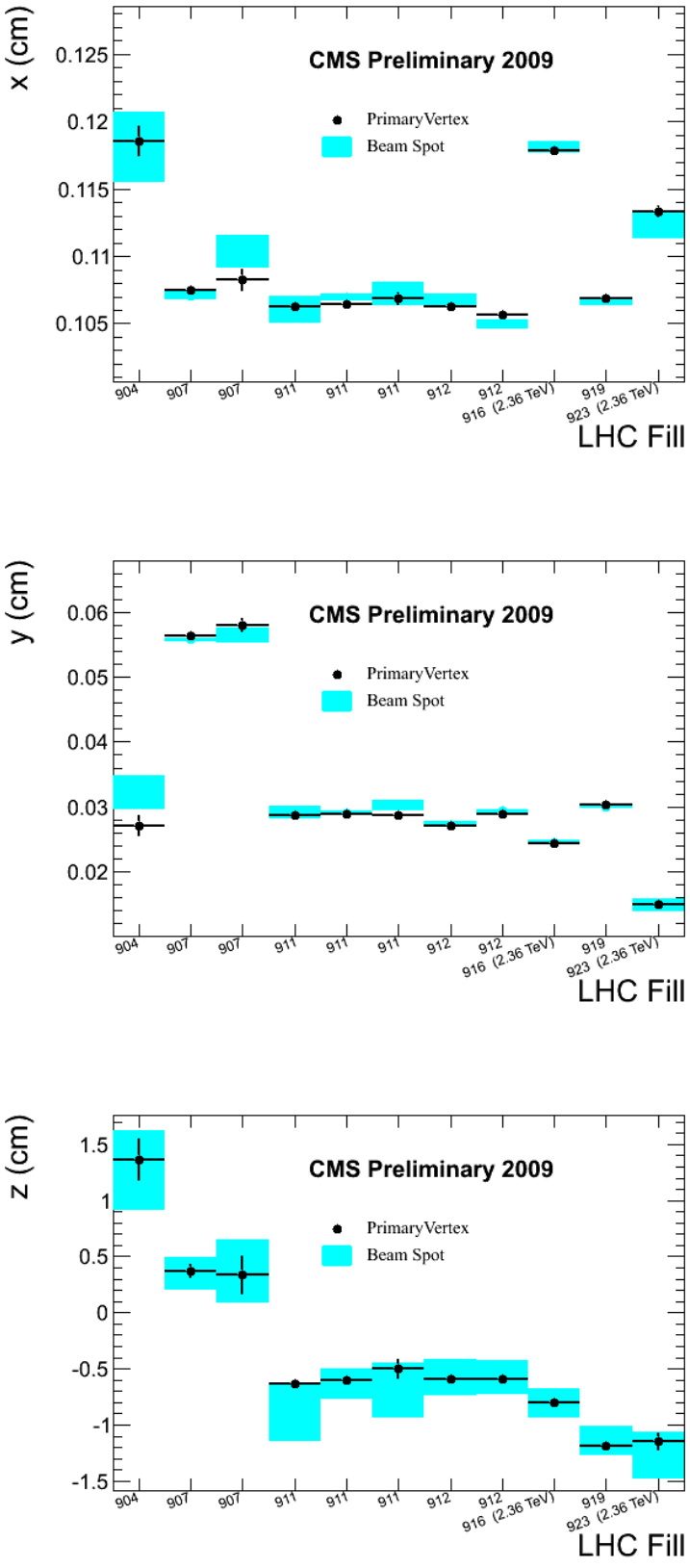

Figure 9: Comparison of fitted x_0, y_0, and z_0 values from the beamspot fit and a gaussian fit to the primary vertex distributions.

distributions and from the beamspot fit. The transverse widths are found to be σ_x ~200 μm and σ_y ~250 μm in the 900 GeV data, consistent with the primary vertex distributions in Fig. 2 and 3, and $\sigma_{x,y}$ ~120 μm in 2.36 TeV data. The observed transverse width is smaller than the values of 293 μm at $\sqrt{s}$ = 900 GeV and 187 μm at 2.36 TeV estimated prior to the start of LHC operations. The difference is understood to be due to the actual machine optics used, compared to what had been used for the projections. The length in z is found to be σ_z ~4 cm in the 900 GeV data and σ_z ~2.8 cm in the 2.36 TeV data.

7 Reconstruction of V^0 Resonances

7.1 Reconstruction and selection

V^0 particles are long-lived ($c\tau > 1$ cm) neutral particles which are reconstructed by their decay to two charged particles: $K^0_S \to \pi^+\pi^-$ and $\Lambda^0 \to p\pi^-$. Reconstruction of V^0 decays requires finding oppositely charged tracks which are detached from the primary vertex and form a good vertex with an appropriate invariant mass. For the Λ^0, the low momentum track is assumed to be the pion. The following selection criteria are applied:

- track requirements:
  - at least 6 hits,
  - normalized track χ^2 less than 5,
  - transverse impact parameter with respect to the beamspot greater than 0.5σ where σ is the calculated uncertainty (including beamspot and track uncertainties),
- vertex requirements:
  - normalized vertex χ^2 less than 7,
  - transverse separation from the beamspot greater than 15σ where σ is the calculated uncertainty (including beamspot and vertex uncertainties),
  - located no more than 4σ inside of the innermost hit of the two daughter tracks where σ is the uncertainty in the vertex position.

7.2 V^0 mass plots

The mass distributions of selected V^0 candidates were used in fits to extract mass shape parameters. The $\pi^+\pi^-$ spectrum was fitted with a double Gaussian (with the same mean) for the signal and a linear background. The $p\pi^-$ spectrum was fitted with a double Gaussian (with the same mean) for the signal and the function $a(m - m_p - m_\pi)^b$ for the background. The data and simulation mass distributions of the K^0_S (Λ^0) candidates are shown in Fig. 10 (11), along with overlaid fits to each distribution. A comparison of masses and resolutions is given in Table 1.

Table 1: Summary of PDG [9], data, and simulation masses and resolutions. The resolution is a weighted average of the core and tail resolutions from the double Gaussian fits. Uncertainties for data and simulation results are statistical only. The masses used in the simulation to generate K^0_S and Λ^0 were 497.670 MeV/c^2 and 1115.680 MeV/c^2, respectively.

	Mass (MeV/c^2)			σ (MeV/c^2)	
V^0	Data	Simulation	PDG	Data	Simulation
K^0_S	497.68 ± 0.06	498.11 ± 0.01	497.61 ± 0.02	7.99 ± 0.14	7.63 ± 0.03
Λ^0	1115.97 ± 0.06	1115.93 ± 0.02	1115.683 ± 0.006	3.01 ± 0.08	2.99 ± 0.03

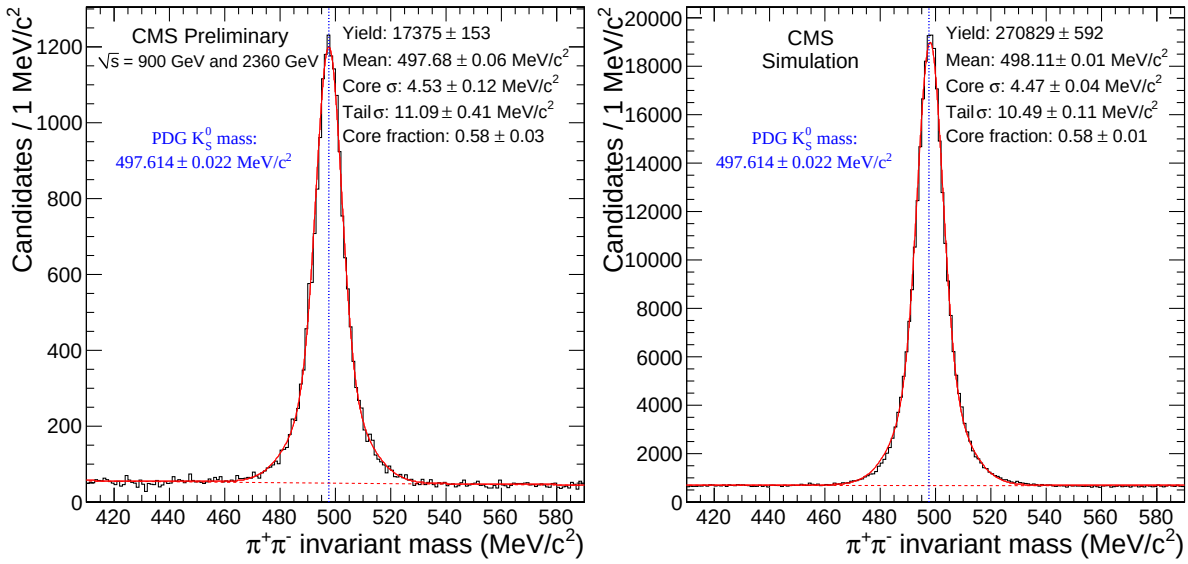

Figure 10: Fitted $\pi^+\pi^-$ mass for data (left) and simulation (right). Uncertainties shown are statistical only.

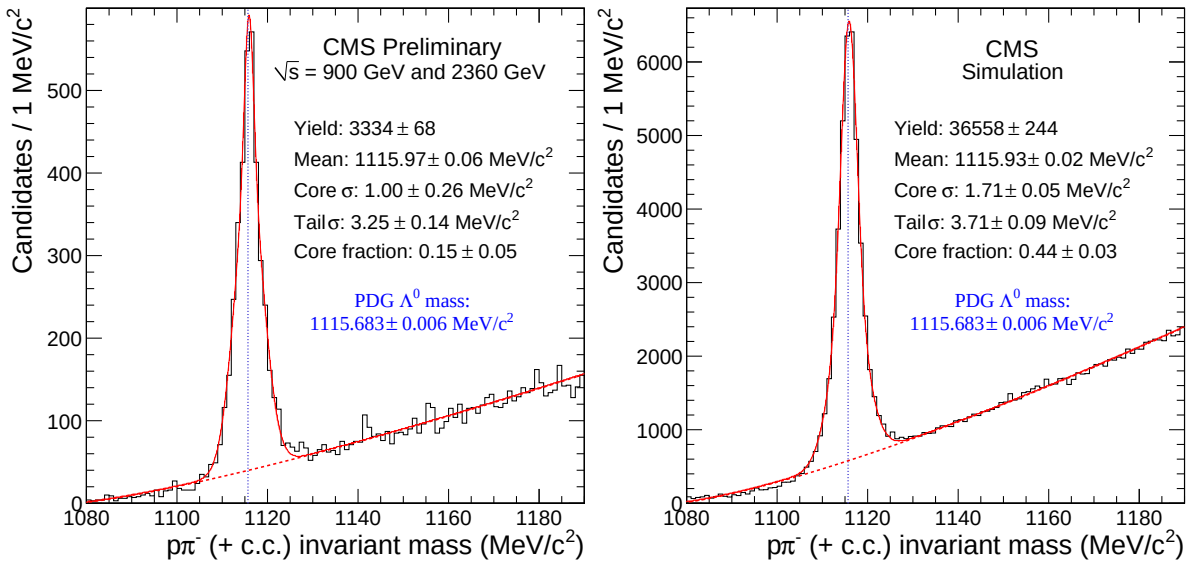

Figure 11: Fitted $p\pi^-$ (+ charge conjugate) mass for data (left) and simulation (right). Uncertainties shown are statistical only.

7.3 Comparison of simulation to data

We can directly compare the data to the simulation by scaling the simulation results. The scale factor used comes from the ratio of K^0_S yields (17375/265320). Applying this scale factor results in the K^0_S and Λ^0 plots shown in Fig. 12. By design, the K^0_S yield matches perfectly. The simulation also reproduces the K^0_S background level fairly accurately, indicating the signal-to-background is consistent between data and the simulation. For the Λ^0 peak, the background is correctly modeled by the simulation but the Λ^0 yield is much lower. This suggests too little Λ^0 production in the simulation relative to K^0_S production. A similar discrepancy between PYTHIA and data in the ratio of K^0_S to Λ^0 production has been observed at CDF [10].

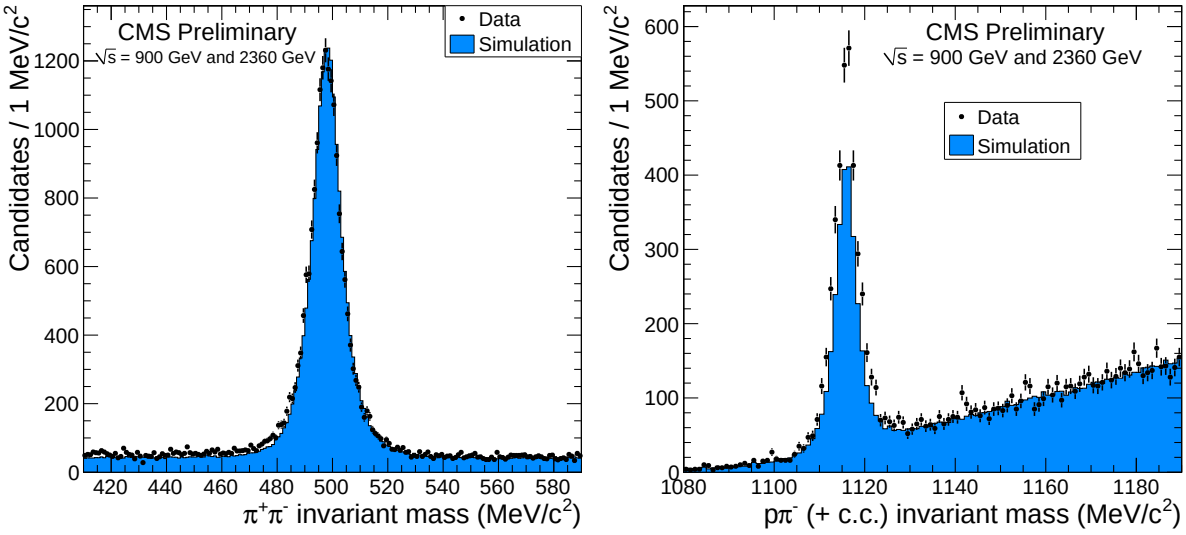

Figure 12: Yield and signal-to-background comparison of K^0_S and Λ^0 between data and simulation. Both simulation histograms are scaled by the ratio of K^0_S yields.

In addition to yields and signal-to-background, we also compare kinematic distributions of the V^0's from the 900 GeV data. The histograms are obtained from a sideband subtraction with a signal region of ± 20 MeV/c^2 (± 7.5 MeV/c^2) about the K^0_S (Λ^0) peak and two sideband regions, each of the same size as the signal region, centered at ± 60 MeV/c^2 (± 22.5 MeV/c^2) away from the K^0_S (Λ^0) peak. Figures 13 and 14 show the comparisons of V^0 pseudorapidity (η), transverse momentum (p_T), momentum, transverse decay length, and decay length for K^0_S and Λ^0, respectively. For each distribution, the simulation histogram is scaled by area to the data histogram.

7.4 V^0 lifetime

For both 900 GeV data and 900 GeV simulated data, mass plots are made in bins of ct where $ct = L/(\beta\gamma) = mL/p$. These mass plots are fitted to extract the yield and the yields are plotted versus ct as the *uncorrected* ct distribution. The uncorrected ct distribution from the simulation is divided by the generated exponential shape given by $e^{-ct/c\tau_{Gen}}$ to obtain the correction factor versus ct. The uncorrected data ct distribution is divided by the correction factor to obtain the corrected ct distribution. This distribution is fitted with a simple exponential, the slope of which gives the measured lifetime.

The uncorrected data ct distribution, the correction factor (from simulation), and the corrected data ct distribution are shown in Fig. 15 for K^0_S and Fig. 16 for Λ^0.

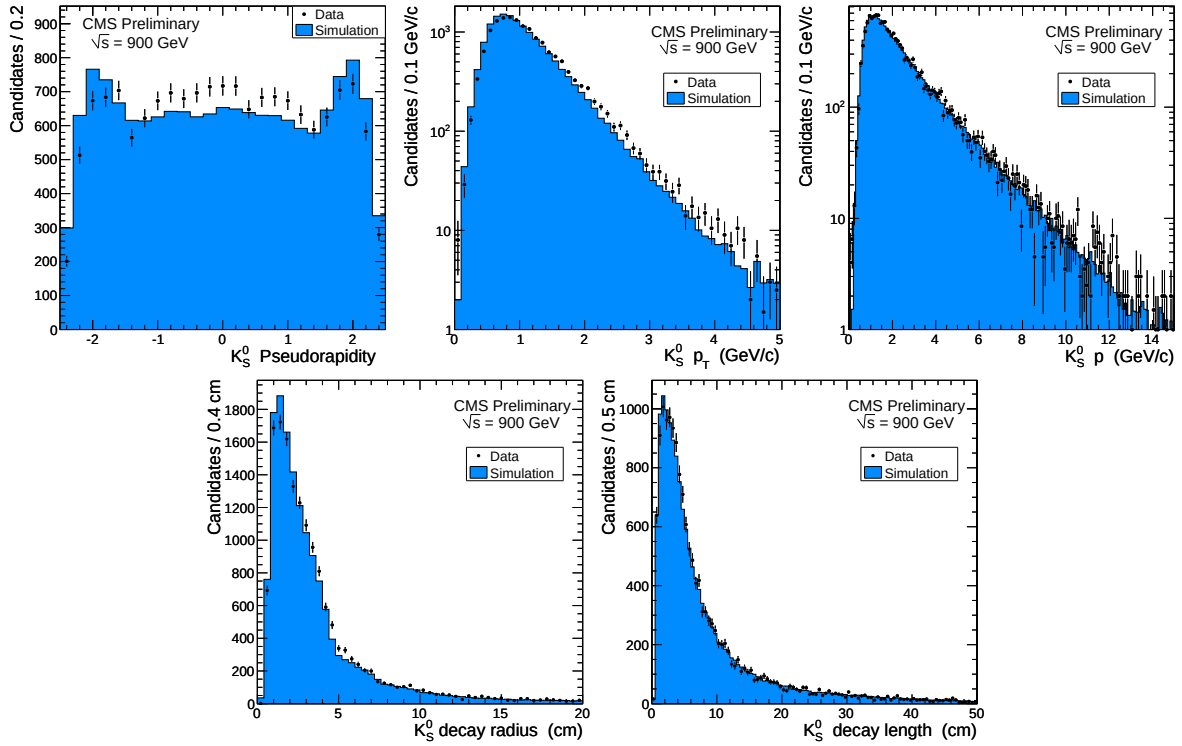

Figure 13: Comparison of various K^0_S kinematic distributions between data and simulation.

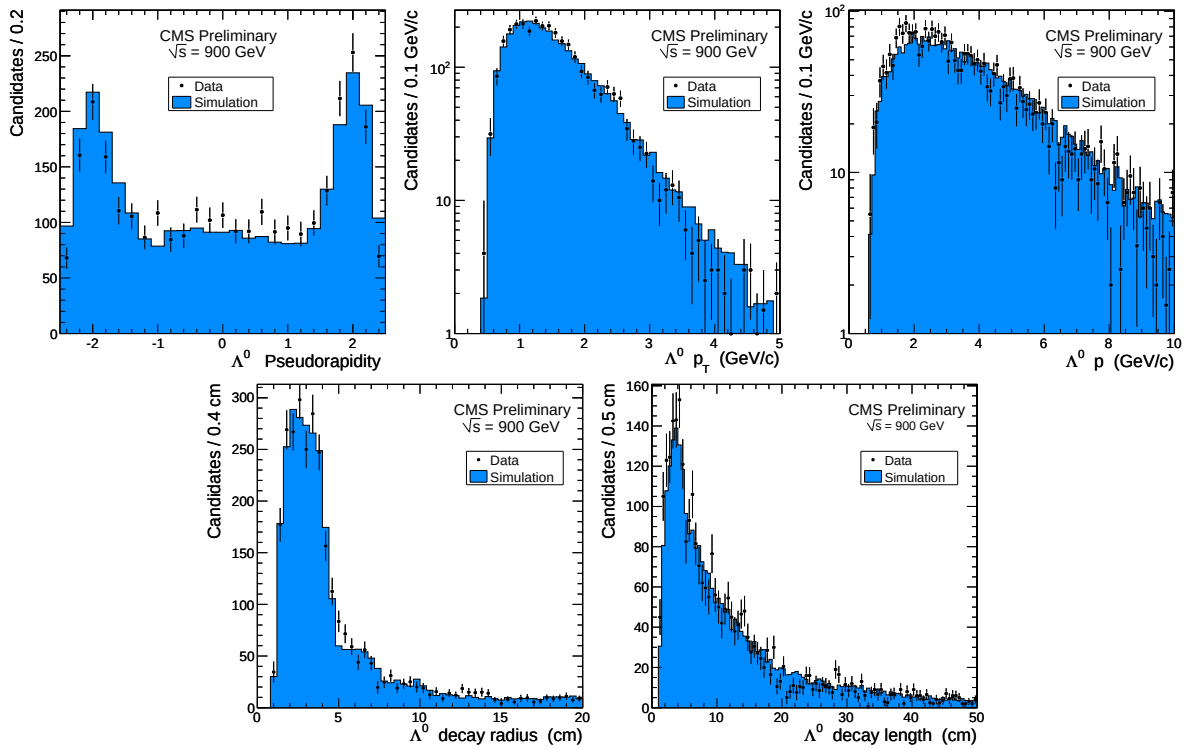

Figure 14: Comparison of various Λ^0 kinematic distributions between data and simulation.

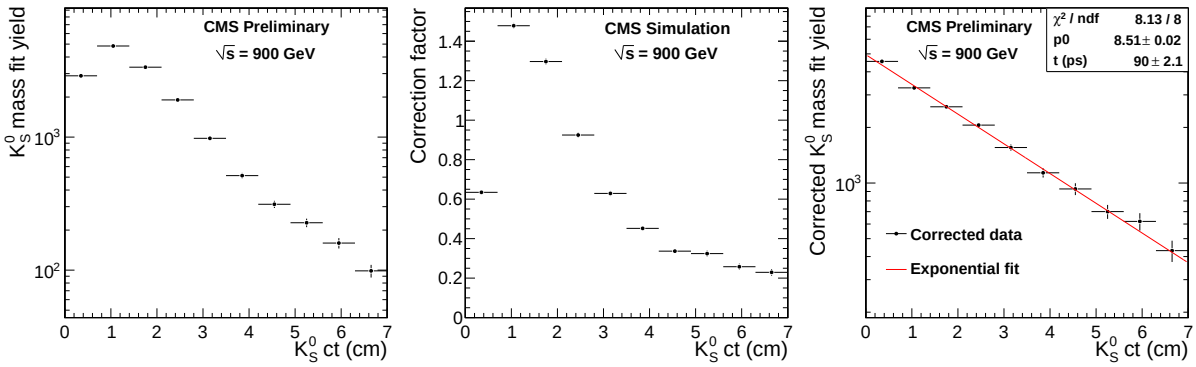

Figure 15: The K^0_S uncorrected *ct* distribution from data (left), the correction factor from the simulation (middle), and the corrected *ct* distribution from data (right) with exponential fit.

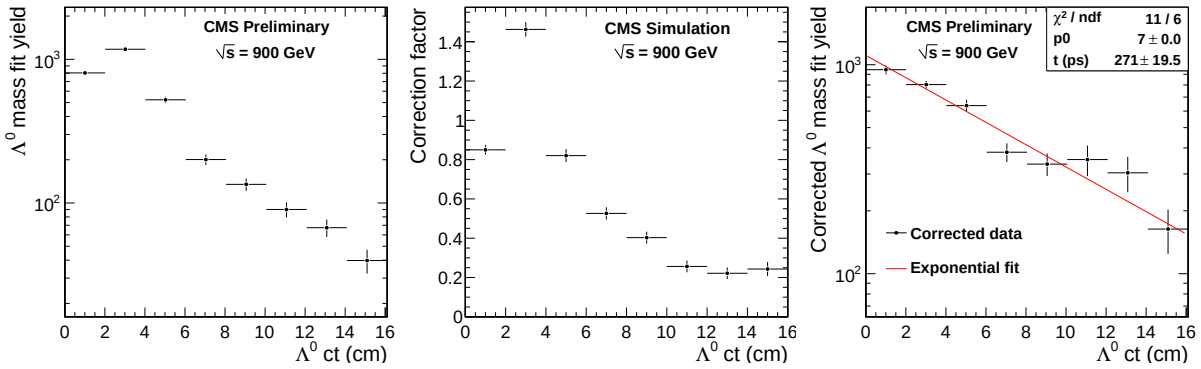

Figure 16: The Λ^0 uncorrected *ct* distribution from data (left), the correction factor from the simulation (middle), and the corrected *ct* distribution from data (right) with exponential fit.

The correction function does a good job of correcting the data as seen by the good fit to an exponential function. The result for K^0_S is $\tau = 90.0 \pm 2.1$ ps, just 0.2σ from the PDG value of 89.53 ± 0.05 ps. The result for Λ^0 is $\tau = 271 \pm 20$ ps, 0.4σ from the PDG value of 263.1 ± 2.0 ps.

7.5 Reconstruction of $\Xi^{\pm}$

The Ξ^- (and, similarly, charge conjugate) is reconstructed through its decay to $\Lambda^0\pi^-$. The data and simulated events were chosen as for the V^0's above. Λ^0 candidates with a mass within 8 MeV/c^2 of the PDG value were selected. For each Λ^0 candidate, charged tracks with the same sign as the pion in the Λ^0 decay were fit with the Λ^0 candidate with a mass constraint applied to the Λ^0. The vertex was required to have a fit probability better than 1%. All three tracks involved in the decay were required to have at least 6 valid hits and a 3D impact parameter with respect to the primary vertex of 3σ. The resulting mass plot, shown in Fig. 17, is fit with a single Gaussian for the signal and a background shape of $Aq^{(1/2)} + Bq^{(3/2)}$ where $q = m - m_\Lambda - m_\pi$. The measured mass of 1322.8 ± 0.8 MeV/c^2 is in agreement with the PDG value of 1321.71 ± 0.07 MeV/c^2. The resolution of 4.0 ± 0.8 MeV/c^2 is close to the simulation result of 3.6 ± 0.4 MeV/c^2. A search for $\Omega^- \to \Lambda^0 K^-$ found no signal.

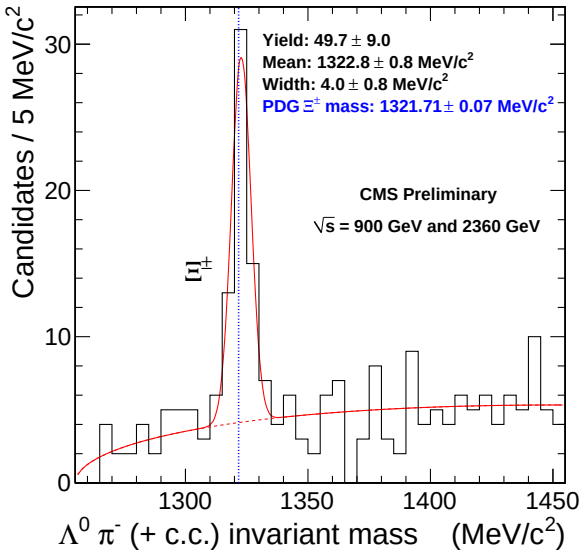

Figure 17: $\Lambda^0\pi^-$ (+ charge conjugate) invariant mass plot with fit for the $\Xi^{\pm}$. Uncertainties shown are statistical only.

7.6 Reconstruction of $K^\star(892)^{\pm}$ resonance

The $K^\star(892)^{\pm}$ resonance is reconstructed in the $K^\star(892)^{\pm} \to K^0_S\pi^{\pm}$ decay channel. Events were required to contain a reconstructed primary vertex consisting of more than two tracks and having a fit probability greater than 0.5%.

The $K^\star(892)^{\pm}$ state is a strong resonance with an extremely short lifetime, hence both K^0_S and $\pi^{\pm}$ candidates are expected to originate from the primary vertex. Neutral vertices are reconstructed using the procedure described in Sec. 7.1. A neutral vertex is accepted as a K^0_S candidate if it meets the following requirements:

- vertex tracks have at least 6 hits;
- the normalized χ^2 of vertex tracks is less than 5;

- the transverse impact parameter significance of each track with respect to the beamspot is greater than 2;
- the normalized χ^2 of the vertex fit is less than 7;
- the transverse distance from the neutral vertex to the beamspot is greater than 15σ;
- the invariant mass of the neutral vertex, assuming that both tracks are charged pions, must be within 20 MeV of the PDG K^0_S mass;
- finally, the three-dimensional impact parameter of the K^0_S candidate with respect to the primary vertex has to be smaller than 2 mm.

The PDG value is assigned for the mass of the reconstructed K^0_S candidate. The three momentum of the K^0_S is calculated as the vectorial sum of the fitted momenta of the vertex tracks at the fitted vertex position. A charged track is regarded as a pion candidate from the $K^{\star}(892)^{\pm} \rightarrow K^0_S\pi^{\pm}$ decay if it is not already assigned to the K^0_S. The selection criteria for tracks are:

- the normalized $\chi^2 < 2$;
- at least two valid hits in the pixel detector;
- at least seven hits;
- transverse momentum $p_T > 0.5\,\mathrm{GeV}/c$;
- pseudorapidity $|\eta| < 2$;
- transverse impact parameter with respect to primary vertex $|d_{xy}| < 2$ mm;
- longitudinal displacement with respect to primary vertex $|d_z| < 3$ mm.

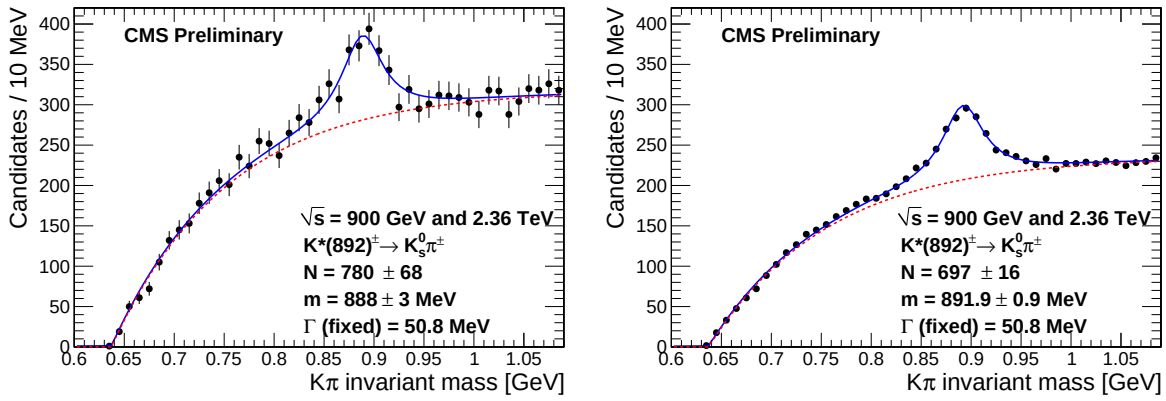

Figure 18: The K^0_S $\pi^{\pm}$ invariant mass distributions in the proton-proton collision data (left plot) and simulation (right plot). The two decay channels, $K^{\star}(892)^{+} \rightarrow K^0_S\pi^{+}$ and $K^{\star}(892)^{-} \rightarrow K^0_S\pi^{-}$, are combined. The simulated distributions of the 900 GeV and 2.36 TeV samples are normalized to the corresponding number of data events selected at 900 GeV and 2.36 TeV, respectively, and added. The dotted lines indicate functions approximating background. The solid lines show results of the fit with the superposition of signal and background distributions. The signal is fitted with the normalization and mass as free parameters.

The three momentum of the charged pion is defined at the point of closest approach of the track to the primary vertex. The PDG value is assigned for the mass of the $\pi^{\pm}$ candidate.

Figure 18 compares invariant mass distributions of $K^{\star}(892)^{\pm} \rightarrow K^0_S\pi^{\pm}$ candidates between collision data and corresponding simulation samples. The distributions of the 900 GeV and 2.36 TeV simulation samples are normalized to the corresponding number of events selected at

900 GeV and 2.36 TeV, respectively, and added. Mass spectra are fitted with the superposition of signal and background distributions. A relativistic Breit-Wigner formula

$$f(m) \sim \frac{1}{(m^2 - M^2)^2 + \Gamma^2 M^2},$$

where m is the $K^0_S\pi^\pm$ invariant mass, M and Γ are the mass and width of the resonance, is used to fit the signal distribution and to determine the yield and mass of the reconstructed state. The background distribution was fitted with the following function

$$b(m) = \mathcal{N} \cdot (1 - \exp \tfrac{m_K + m_\pi - m}{p}),$$

where m_K and m_π are PDG values of the K^0_S and $\pi^\pm$ masses, respectively. The fit of the background distribution is performed with the normalization $\mathcal{N}$ and variable p as free parameters. For $m < m_K + m_\pi$, the background function is set to zero.

The fit of the signal distribution is performed with the normalization and mass as free parameters. The width is fixed to the $K^\star(892)^\pm$ PDG value of 50.8 MeV [9]. Signal properties are summarized in Table 2. The fitted masses are consistent with the PDG value [9] within statistical uncertainties. The number of $K^\star(892)^\pm$ candidates in collision data is 1.2σ above the prediction from simulation.

Table 2: Summary of signal properties. Fitted values for yield and mass.

	$K^\star(892)^\pm \to K^0_S\pi^\pm$		
	Data	Simulation	PDG
Mass (MeV/c^2)	888±3	891.9±0.9	891.66±0.26
Width (MeV/c^2)	50.8 (fixed)	50.8 (fixed)	50.8±0.9
Candidates	780±68	697±16	

We also studied distributions of the $K^\star(892)^\pm$ transverse momentum p_T, pseudorapidity η, and azimuthal angle ϕ. The sideband background subtraction technique was exploited to reconstruct the p_T, η and ϕ spectra of $K^\star(892)^\pm$ candidates. The central band in the reconstructed $K^\star(892)^\pm$ mass spectrum is chosen to be centered at the fitted value of the $K^\star(892)^\pm$ mass. The edges of the central band are adjusted to ensure containment of 85% of signal events. Sidebands are defined in such a way that the number of events in each sideband equals half of the number of background events in the central band. The ranges for the central band and sidebands are summarized in Table 3.

The final distributions are reconstructed by subtracting the p_T, η and ϕ spectra obtained for sidebands from the spectra obtained for the central band. The background subtracted distributions for the collision data and simulation samples are compared in Fig. 19. The distributions are not unfolded with the p_T and η dependent corrections for the signal efficiencies. Observed data are in good agreement with predictions from simulation.

Table 3: Central (signal) and sidebands in the distribution of the $K^0_S\pi^\pm$ invariant mass for the data and simulation samples. These ranges were used to reconstruct the p_T, η and ϕ spectra of $K^\star(892)^\pm$ candidates exploiting a sideband background subtraction technique.

	Left band (MeV/c^2)	Central band (MeV/c^2)	Right band (MeV/c^2)
Data	702−811	811−966	966−1037
Simulation	709−815	815−970	970−1039

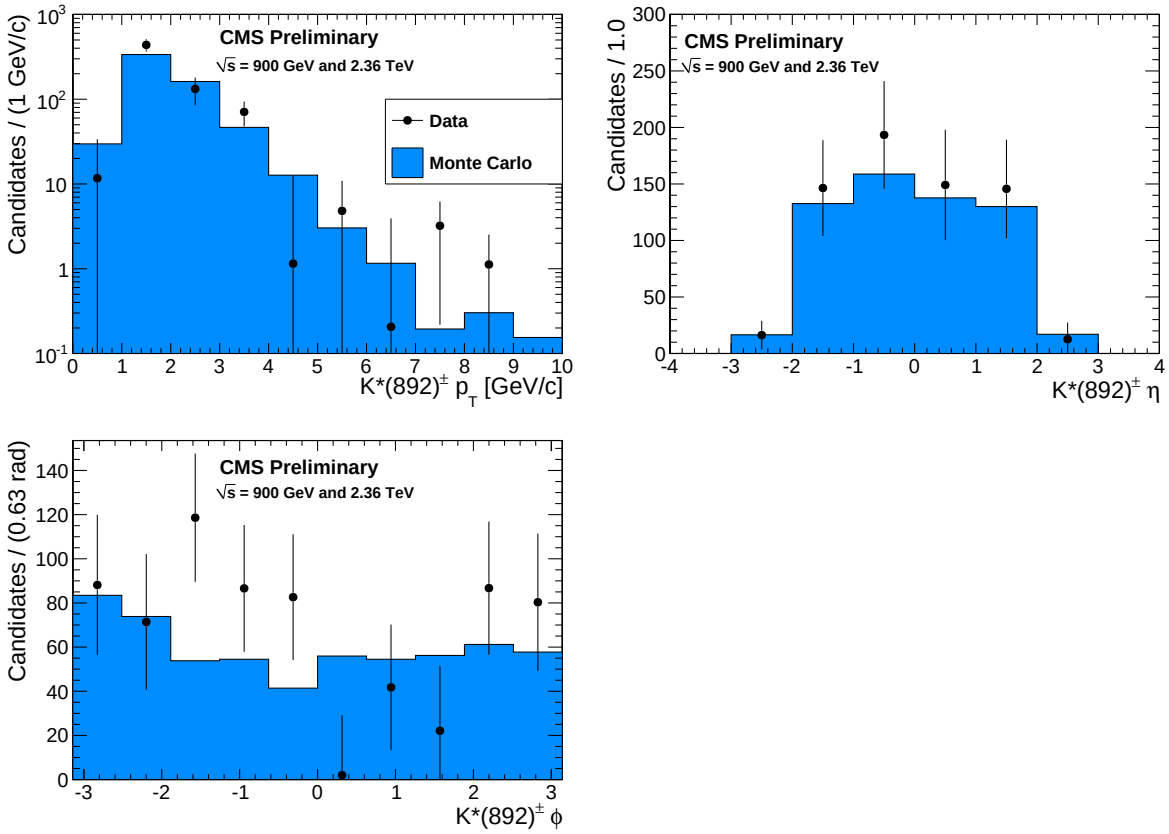

Figure 19: Distributions of $K^{\star}(892)^{\pm}$ p_T (upper-left plot), η (upper-right plot) and ϕ (lower plot) in the proton-proton collision data (dots) and simulation (filled histograms). The two decay channels, $K^{\star}(892)^{+} \rightarrow K^{0}_{S}\pi^{+}$ and $K^{\star}(892)^{-} \rightarrow K^{0}_{S}\pi^{-}$, are combined. The distributions of the 900 GeV and 2.36 TeV simulation samples are normalized to the corresponding number of data events selected at 900 GeV and 2.36 TeV, respectively, and added.

8 Particle Identification with dE/dx

Specific ionization energy loss is a powerful observable for particle identification. One such application will be shown in Sec. 9, and with higher-energy collisions it will be used as one of the main handles for the search for new charged long-lived particles [11].

In the following the generic notation dE/dx will be used to indicate the ratio between the charge (or energy) released by a charged particle and the distance it traveled across the sensitive volume of a silicon strip sensor. The same notation will also be used to indicate the specific ionization produced by a particle.

This part of the analysis is restricted to the data sample in collisions at 900 GeV. The following selection was applied at track level, before the computation of the particle dE/dx:

- the track has to be flagged as *highPurity*;
- it must have at least 10 hits in the silicon strip tracker;
- it must be loosely compatible with the primary vertex in the transverse ($|d_{xy}| < 2$ cm) and longitudinal ($|d_z| < 15$ cm) directions.

The fake track rate for this selection is negligible, as estimated from simulation.

The most probable value of the particle specific ionization energy loss can be estimated by means of one of the estimators documented in [12]. In this paper results are shown for a generalized mean of the hit charges per unit path length traversed in the silicon (c_i for the i-th hit attached to a given reconstructed track), defined by

$$I_h = \left(\frac{1}{N} \sum_i c_i^k \right)^{1/k} \tag{2}$$

with $k = -2$. Hit charges are corrected by an equalization factor computed at module level by means of high-momentum particles ($p > 1$ GeV/c, at least 8 hits), and expressed in MeV/cm by applying a conversion factor extracted from cosmic data [13]. The short-hand notation dE/dx is used for this estimator.

An estimate of the mass of each candidate passing the selection described above can be obtained using the particle momentum and the measurement of the ionization energy loss provided by the dE/dx estimators. To this end the following relation between dE/dx, p and m is assumed for the momenta below the minimum-ionizing region:

$$\frac{dE}{dx} = K\frac{m^2}{p^2} + C \, . \tag{3}$$

Figure 20 shows the distribution of dE/dx versus p for particle-calibrated data and simulation for the estimator considered. The bands departing toward high dE/dx values at low momentum are attributed to kaon, proton and deuteron tracks. In this study, the proton line is used to extract the parameters K and C in Eq. 3. The fit to the proton band is restricted to the range $[0.7, 1.0]$ GeV/c and shown as a red curve in Fig. 20, while the black curves show that the same K and C values yield a good agreement also for charged kaons and for protons of lower and higher momentum.

The mass spectrum resulting by inverting Eq. 3 for all tracks with $dE/dx > 4.15$ MeV/cm and $p < 2$ GeV/c is shown in Fig. 21. The known values of the kaon and proton masses are also indicated as vertical lines on the plot. We observe an additional peak in data which is not visible in simulation, and we attribute it to deuterons.

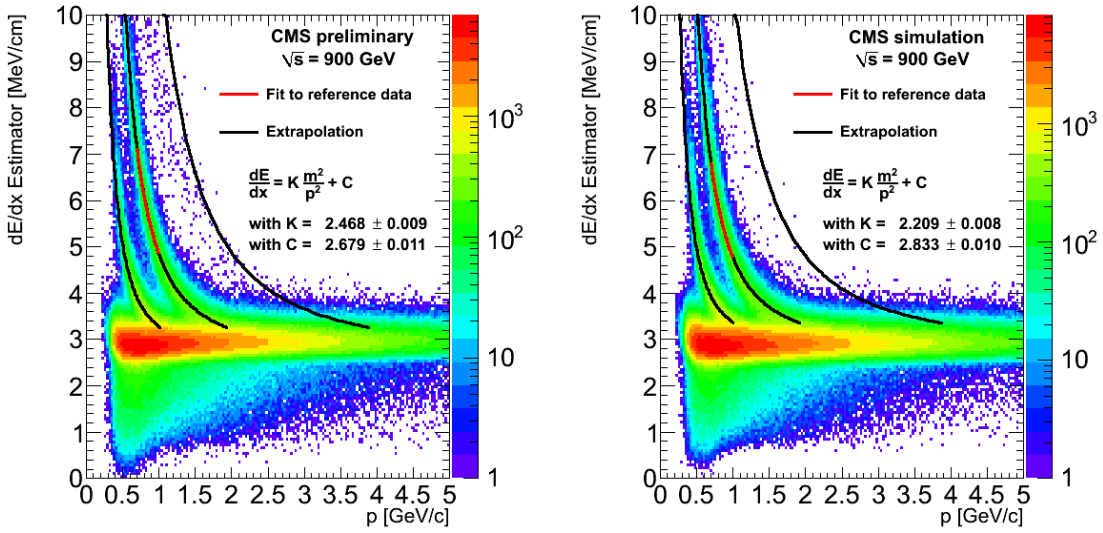

Figure 20: dE/dx versus p in data collected at 900 GeV during December 2009 (left) and simulation (right); red line: fit with proton mass assumption, in a restricted p range; black lines: extrapolations.

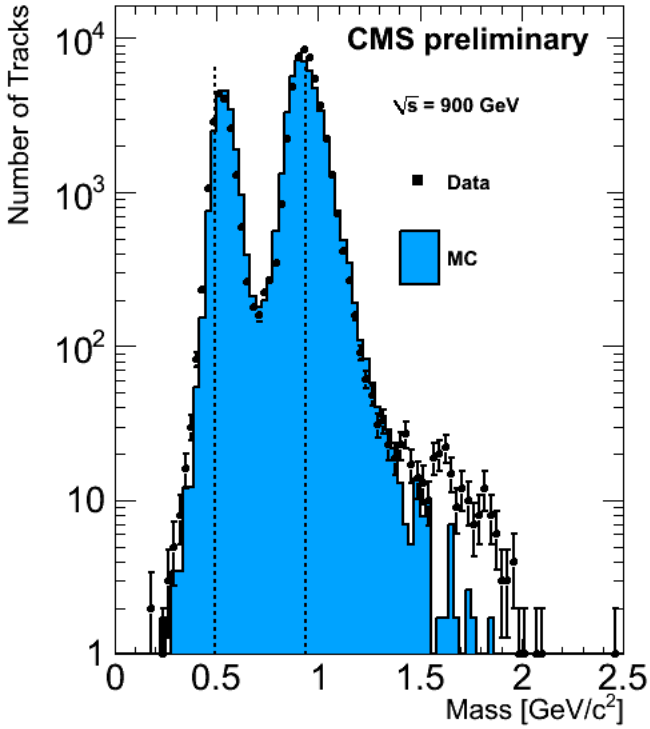

Figure 21: Mass distribution, as defined from Eq. 3, for tracks with $p < 2$ GeV/c and $dE/dx >$ 4.15 MeV/cm for 900 GeV data (dots with error bars) and simulation (solid).

We validate the dE/dx measurement for protons using reconstructed $\Lambda^0 \rightarrow p\pi$ decays. The kinematics of this two-body decay implies [14] that the proton is the higher momentum particle in the pair whenever p_Λ is above approximately 300 MeV/c, which is true for reconstructed Λ^0s in our sample as seen in Fig. 14.

We apply the same selection as in Section 7, and we plot the dE/dx distribution as a function of momentum for tracks associated to Λ^0 candidates in the mass range $[1.08 - 1.16]$ GeV/c^2, separately for the higher (left) and the lower (right) momentum track in the pair in Fig. 22.

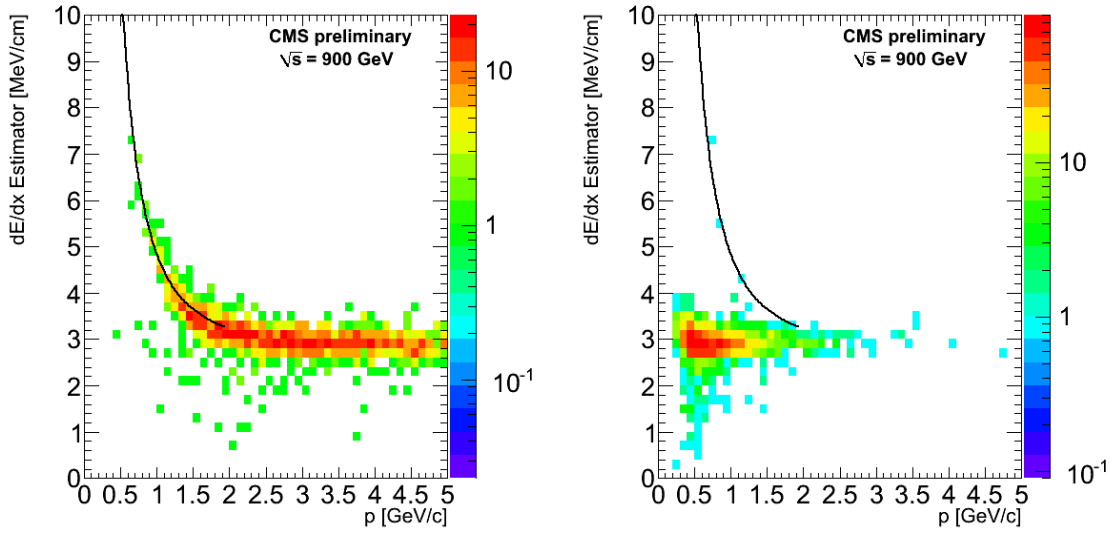

Figure 22: dE/dx of the leading (left) and softest (right) tracks associated to Λ^0 candidates. The superimposed curve comes from the proton fit in the inclusive track sample.

9 Reconstruction of $\phi(1020) \rightarrow K^+K^-$

The $\phi(1020)$ resonance is searched for through its decay into two charged kaons. We only analyze data taken at $\sqrt{s} = 900$ GeV. We collect $\phi(1020) \rightarrow K^+K^-$ candidates in events with less than 150 tracks with candidate kaons selected from *highPurity* tracks passing the following requirements:

- $p_T > 0.5$ GeV/c;
- normalized $\chi^2 < 2.0$;
- at least 5 hits;
- $|\eta| < 2.0$;
- transverse impact parameter with respect to reconstructed beam spot $|d_{xy}| < 0.3$ cm;
- $p > 1$ GeV/c or dE/dx corresponding to M in the range of $M_K \pm 200$ MeV/c^2 following the relationship in Eq. 3 with K and C parameters determined in Sec. 8.

Figure 23 shows the selection of tracks on the basis of dE/dx for the simulation and data samples.

Finally, we form all possible track pairs of opposite curvature in each event.

We fit the mass spectra of pairs of tracks accepted by the dE/dx selection using the sum of two normalized functions: a Voigtian (convolution of a relativistic Breit-Wigner shape and a

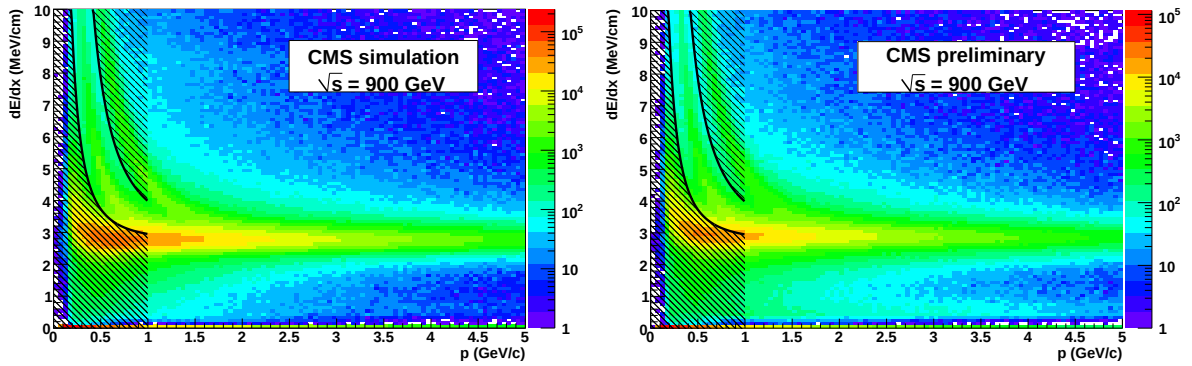

Figure 23: Energy loss in the simulated sample (left) and in the data sample (right) per track as a function of track momentum, for all tracks. The requirements described in the text remove the hatched grey areas.

Gaussian smearing) for the ϕ signal, and a simple arctangent form for the background.

We first fit the distribution found in the simulation by fixing the natural width of the $\phi(1020)$ resonance to the value used to generate the simulated events, i.e. 4.458 MeV/c^2 [15].

We next fit the mass distribution found in the data. We test whether the fit to experimental data can recover a mass resolution in agreement with simulation expectations, by leaving the resolution term free in the fit, while fixing the natural width of the resonance to the current value ($\Gamma_\phi = 4.26$ MeV/c^2 [9]).

The results of both fits are listed in Table 4 and shown in Fig. 24. The measured ϕ mass of 1019.58 ± 0.22 MeV/c^2 is consistent with the world average value of 1019.455 MeV/c^2 [9]. Also the observed ϕ mass resolution of 1.29 ± 0.32 MeV/c^2 is in very good agreement with simulation expectations.

Table 4: Summary of $\phi(1020) \rightarrow K^+K^-$ signal properties.

	Data	Simulation	PDG
Mass (MeV/c^2)	1019.58±0.22	1019.74±0.13	1019.455±0.020
Sigma (MeV/c^2)	1.29±0.32	1.41±0.22	
Width (MeV/c^2)	4.26 (fixed)	4.458 (fixed)	4.26±0.04
Candidates	1728±102		

To check the goodness of the dE/dx selection, we show in Fig. 25 for simulation and data the mass distribution of all the opposite-curvature track pairs passing the selection criteria discussed in this section, but with at least one track failing the dE/dx selection. While the presence of the $\phi(1020)$ signal is clear in the distributions passing the dE/dx requirement, it is not evident in the ones failing.

10 Reconstruction of Photon Conversions

The performance of the CMS Pixel and Silicon Tracker detectors described so far was achieved at the price of a substantial material budget (up to 1.8 X_0). The direct consequence is that a large fraction of photons convert into e^+e^- pairs while traversing the Tracker material and in addition electrons have a high probability to emit Bremsstrahlung. In the Minimum Bias

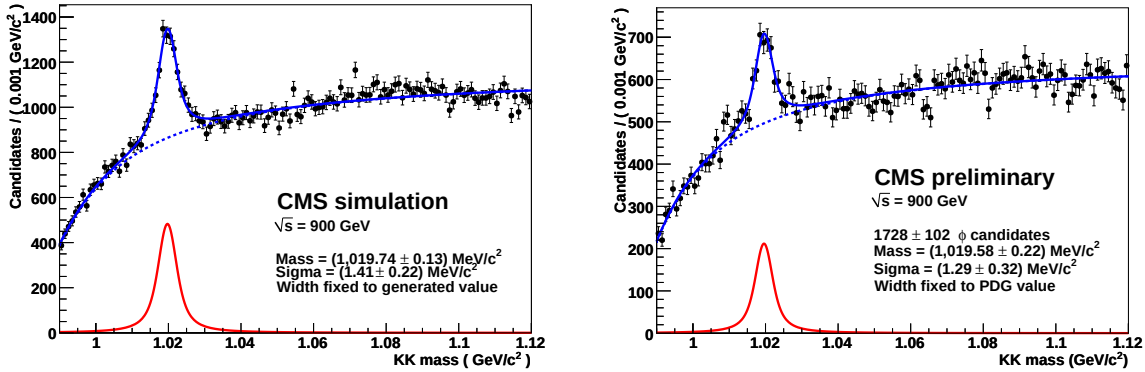

Figure 24: Fit to the mass distribution of kaon candidate pairs in simulation (left) and in data (right). The natural width is fixed to the generated value for simulation and to the current value, $\Gamma_\phi = 4.26$ MeV/c^2, for data.

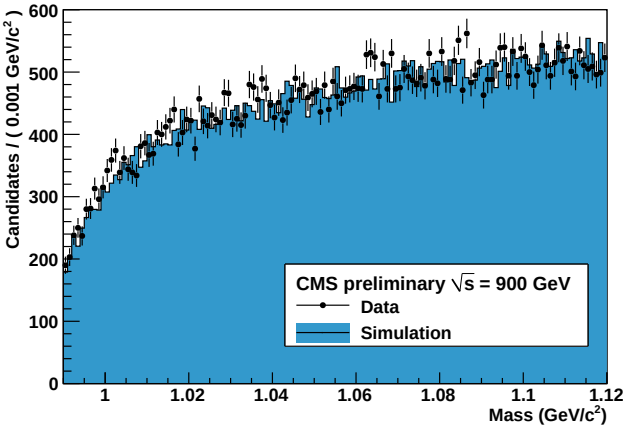

Figure 25: Mass distribution of kaon candidate pairs in simulation (blue area) and in data (points), when at least one track fails the dE/dx requirement.

events collected during the very first phase of CMS data taking, photons, mainly coming from π^0 decays, are expected to have a very soft spectrum. The conversion electron pairs are very unlikely to reach the ECAL and the ECAL-driven track and seed finding method [16] cannot be applied. The recent development of the iterative tracking described in Sec. 2 greatly extends the capability of reconstructing very low-p_T tracks which are exploited here for conversion identification.

10.1 Selection and results

The essential signature which is sought is the massless photon which corresponds to two tracks parallel at the production vertex, both in the transverse and in the longitudinal plane. Oppositely charged tracks then open only in ϕ due to the magnetic field. The results in this analysis summary have been obtained following two different approaches, both aiming at achieving high efficiency while keeping the purity at a reasonable level. The first approach, is based on a simple track pair pre-selection; opposite-sign track pairs are required to satisfy quality criteria (one track must have ≥ 5 hits, the other track must have ≥ 3 hits, and both tracks should have normalized $\chi^2 < 10$), and then the tracker-only conversion finding exploits the conversion pair signature to distinguish genuine pairs from fake pairs. Tracks are required to have positive charge-signed transverse impact parameter, positive distance of minimum approach in 2D (i.e. the two full track circles have one or no intersection in the transverse plane), small z separation at their innermost point ($|\Delta z| < 5$ cm) if they are in the barrel, and a small opening angle in both the transverse ($\Delta\phi < 0.2$) and longitudinal plane ($\Delta \cot\theta < 0.1$).

Track pairs surviving the selection are then fitted to a common 3D-constrained kinematic vertex fitter. The 3D constraint imposes that tracks be parallel at the production vertex in both transverse and longitudinal planes. The pair is retained if the fit converges and its χ^2 probability is greater than 5×10^{-3}. After the vertex fit, it is also required that no hits are present before the vertex position along the tracks. Figure 26 shows the level of agreement found between data and simulation for some of the discriminating variables used in the selection. Figure 27 shows the pair invariant mass distribution.

The tracker material distribution is illustrated in Fig. 28, where the pseudorapidity and ϕ distributions for all selected tracks are shown. Here and in the remainder of this section, the distributions are normalized to the number of selected candidates in data.

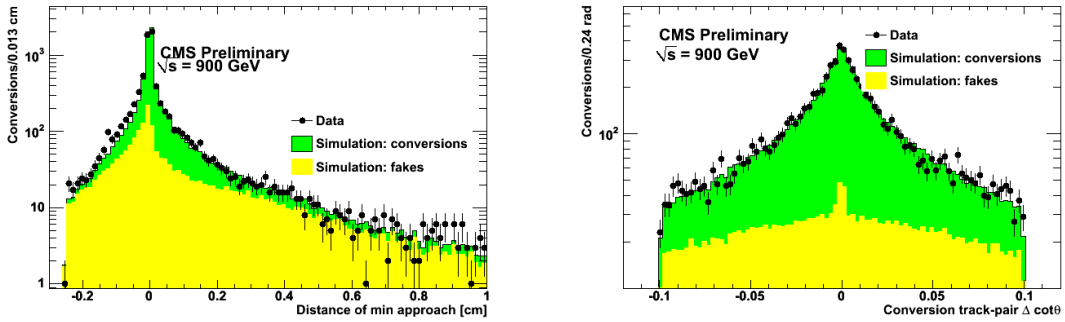

Figure 26: Distance of minimum approach between the tracks (left) and angular separation in the longitudinal plane, $\Delta \cot\theta$, of tracks (right). The expected contribution from fakes is also shown.

A significant result is the first Tracker radiography (Fig. 29) and the corresponding distribution of the radial position for reconstructed conversion vertices. Since the 900 GeV data have a very

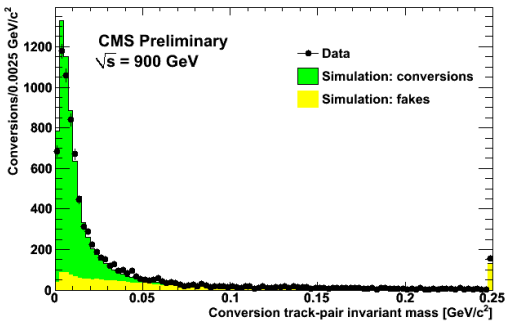

Figure 27: Electron-positron invariant mass. The expected contribution from fakes is also shown. The last bin of the histogram collects the overflows.

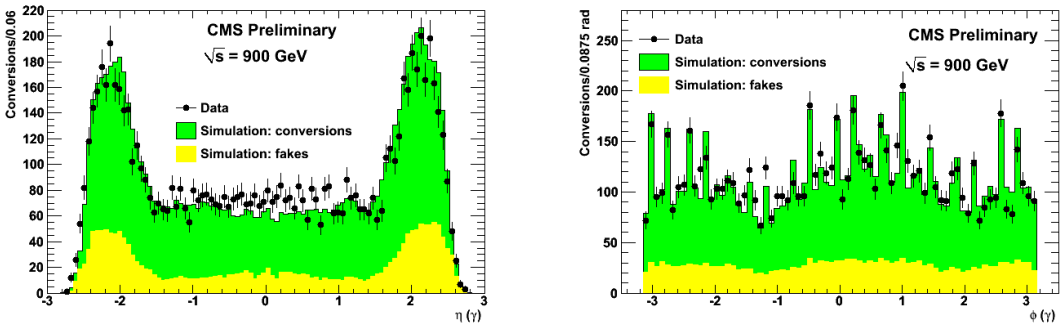

Figure 28: Pseudorapidity distribution and ϕ distribution for all conversion candidates, as reconstructed from the track-pair momentum. The contribution expected from fakes is also shown.

soft p_{T} spectrum, most of the conversions occur in the beam pipe (3 cm radius) or in the first pixel layer (4.4 cm radius). Due to an offset between the beam pipe and the pixel detector, we chose to calculate the coordinates with respect to the center of the pixel detector. The double-peak structure is due to the ladder in the first pixel layer; the beam pipe is smeared out because of the radial resolution and in data also because of the different reference frame used. The 18-fold structure visible in (x, y) view of the first pixel layer is due to the cooling pipes, smeared out by the radial position resolution of the conversion vertex, which is expected to be about 0.5 cm from simulation. The same structure is also visible in Fig. 28.

The second conversion reconstruction approach is based on a minimal track-pair pre-selection aiming at larger efficiency coming at the cost of lower purity; only opposite-sign tracks with a track-fit χ^2 probability greater than 10^{-6} are considered and fitted to a common vertex [17] also applying a 3D parallelism constraint on the track pair. The results are therefore sensitive to small changes in the helix parameters of the tracks or associated covariance matrices. Conversion candidates are retained if the conversion vertex fit probability is greater than 10^{-6} and they have a positive decay length in the $x - y$ plane. It is also required that no more than one hit per track is present before the vertex position. Finally only conversions occurring at a radius greater than 2.0 cm are considered good conversion candidates. Despite the loose selection criteria, the three-dimensional conversion constraint makes the conversion fit probability cut (Fig. 30) quite powerful for selecting good conversion candidates.

The agreement between data and simulation in the fit probability distribution demonstrates

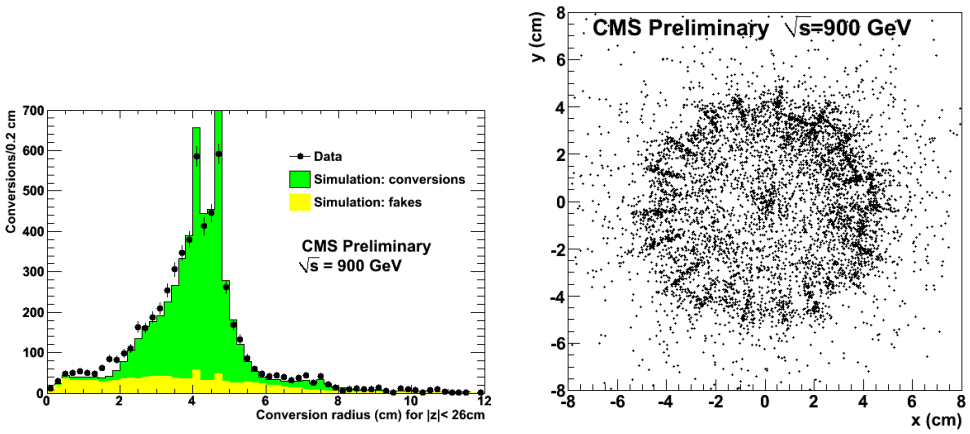

Figure 29: Conversion vertices: distribution of the radial position (left) and (x, y) view of conversion vertices for $|z| < 26$ cm, i.e. pixel barrel (right). Because of the offset between the beam pipe and the pixel detector, the radius is calculated with respect to the center of the pixel detector

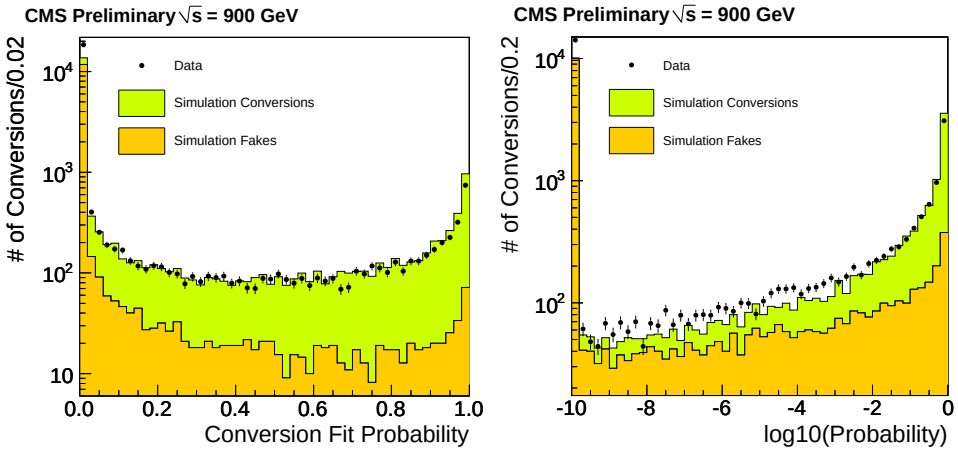

Figure 30: Distribution of the vertex χ^2 probability obtained with CTVMFT (left). The same distribution is plotted with a logarithmic x-axis (right) where the low-probability region can be seen in more detail. These plots are made with all other selection cuts applied aside from the probability cut itself, and therefore exclude candidates with radius < 2.0 cm.

that the track parameters and uncertainties are already reasonably well simulated, even for lower quality tracks. The distribution of the radial position for conversion vertices obtained with the second approach is shown in Fig. 31 together with the (x, y) view. A major remaining source of disagreement between data and simulation is the known global offset on the order of a few mm, visible in the data between the beam pipe and the first pixel barrel layer, which is not currently represented in the simulation.

10.2 Material estimation from data

The number of reconstructed photon conversions can be used to estimate the amount of material in the beam pipe and in the tracker, if the reconstruction efficiency and the photon flux are known. In particular, assuming a negligible background, the number of reconstructed photon

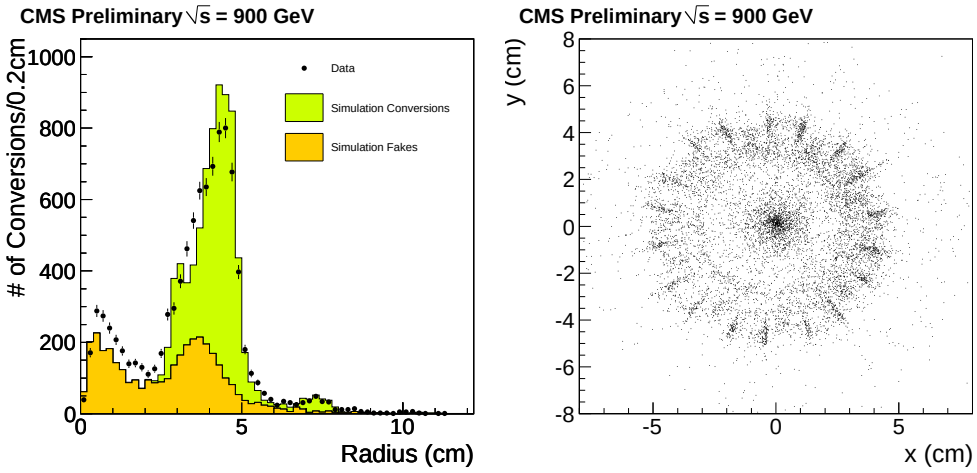

Figure 31: Conversion vertices: distribution of the radial position with respect to the nominal pixel center (left) and (x, y) view of conversion vertices (right), both restricted to $|z| < 26$ cm, i.e. pixel barrel. These plots are made with all selection cuts applied aside from the $r > 2.0$ cm requirement.

conversions N_{reco} in a given volume bin is

$$N_{\text{reco}} \propto \varepsilon \cdot \frac{P}{X_0} \cdot f_{\text{geom}} \tag{4}$$

where ε is the reconstruction efficiency, P/X_0 is the average conversion probability ($P \sim 7/9$), and f_{geom} is a factor from the integration of the geometrical dependence and the photon flux over the volume bin. The photon flux is assumed to be flat in η, to scale as $1/R^2$ and to originate from $(0, 0, 0)$. With these assumptions the proportionality becomes $1/(R^2 \sin\theta)$.

The present event sample only provides enough data for the study of the material within the two innermost layers of pixel barrel detector. This region is identified by choosing the following fiducial volume: $|z| < 26$ cm and $r < 8.8$ cm. For convenience, r is divided further into three parts, corresponding to the beam pipe and the pixel layers: $2\text{ cm} < r_{\text{BP}} < 3.2\text{ cm} < r_{\text{PXL1}} < 6\text{ cm} < r_{\text{PXL2}} < 8.8$ cm. The conversion finding efficiency ε, estimated from Monte Carlo for each sub-region, is 2.6%, 3.5%, and 0.5% respectively. In collision data ~ 2300 conversions are selected after quality cuts designed to guarantee a good balance between purity and efficiency. On top of the quality requirements of the first approach, described in Section 10.1, both legs are required to have at least four hits and the positive charge-signed transverse impact parameter larger than 0.1 cm. Simulation data are normalized to the total number of collision events after trigger and good vertex selection. The overall agreement on the number of conversions is within 10%.

Figure 32 represents an uncalibrated estimation, given in arbitrary units, comparing the material distribution of the beam pipe and of the first two pixel barrel layers. The distribution of the conversion vertex radius from the simulation truth, corrected for f_{geom}, represents the case of ideal efficiency and resolution (green histogram). Blue boxes and black dots represent simulation pseudo-data and data respectively, both corrected for ε and f_{geom}. These distributions are smeared with respect to simulation truth as a consequence of the vertex radius resolution. The conversion radius in data is the distance from the pixel center. The expected fake contribution, shown in red boxes, is not subtracted. Data show a good agreement with simulation

pseudo-data, both in shapes and in the overall number of entries.

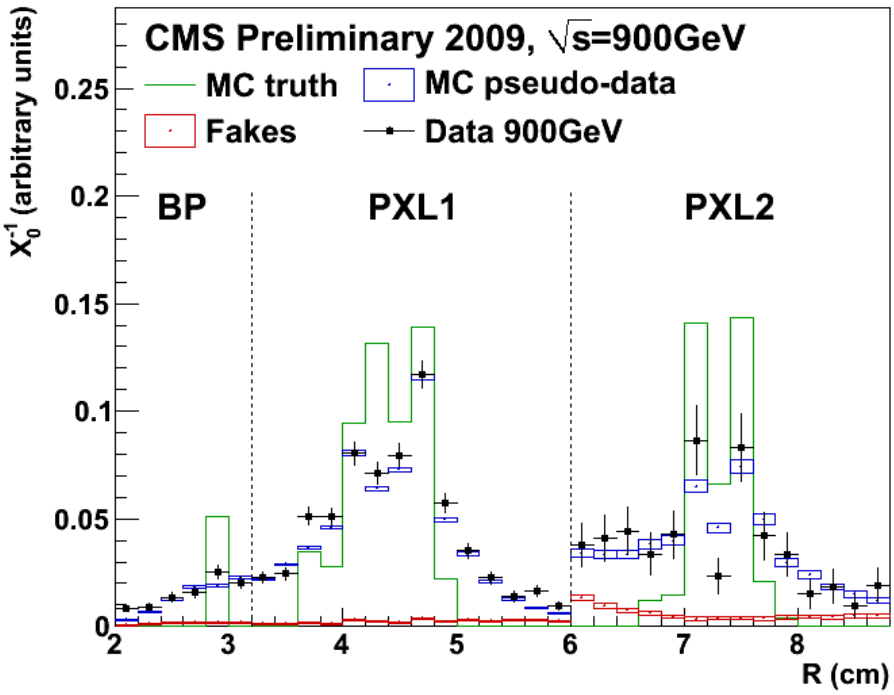

Figure 32: Uncalibrated material distribution as a function of the radius.

11 Reconstruction of Nuclear Interactions

The problem of nuclear interactions in the tracker is similar in many ways to photon conversions as described above in Sec. 10. The overall material distribution of the silicon tracker varies between $0.1 - 0.5\ \lambda$, where λ is a characteristic nuclear interaction length [18]. Simulation shows that typically 5% of the charged pions with $p_T \approx 5$ GeV interact in the tracker. Thus at the center-of-mass energy of 14 TeV dozens of those interactions are expected to be produced in each QCD event. They affect the resolution of many hadronic observables such as jets or missing transverse momentum.

There are two complementary strategies to correct at least partially the nuclear interaction effects: event-by-event correction and average correction with the simulation. Both approaches employ the reconstruction of nuclear interactions based on tracks. On the one hand the reconstructed nuclear interactions may be used to improve the reconstruction of the event where it was observed. On the other hand a comparison of distributions of nuclear interactions in the data and in the simulation allows us to improve our understanding of the material distribution and density in the silicon tracker and its possible variations in time. The aim of this analysis was to use the first hadrons propagating through the CMS tracker to test the compatibility between the actual tracker geometry and its simulation.

The nuclear interactions finder is fully based on the tracker information. The finding procedure starts from the list of iterative tracks described in Sec. 2 with a loose selection. For each pair of tracks a distance, namely the distance of closest approach, is computed. Two tracks close

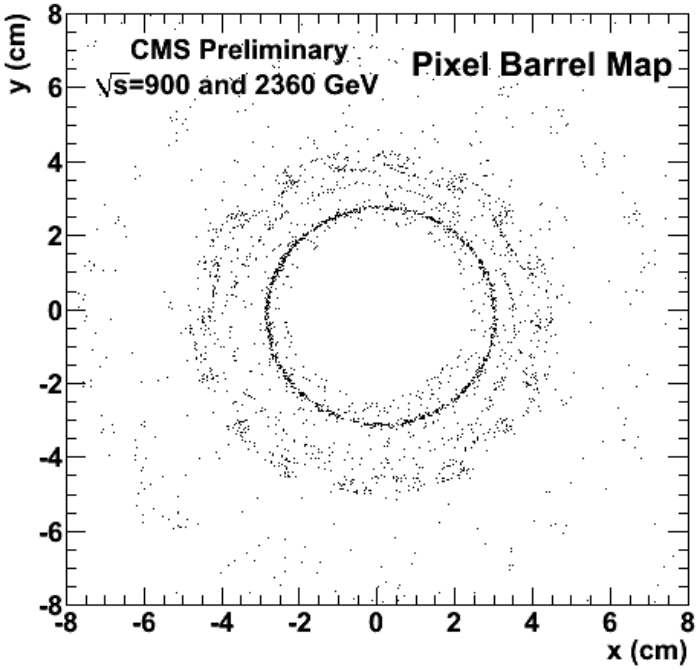

Figure 33: The nuclear interaction vertices: distribution in the (x, y) plane, for $|z| < 26$ cm obtained with Minimal Bias data.

enough together are considered as linked together. A recursive finder produces then blocks of tracks linked together. A rough estimate of the displaced vertex position is computed from a weighted average of points of closest approach of all the possible pairs of tracks from the block. In a last step the tracks from a block are refitted together with a displaced vertex as a common constraint.

Displaced vertices consistent with V^0 decays and conversions, as identified in Sec. 7 and Sec. 10 are removed from the sample. A tight selection is applied to the remaining vertices to remove fake tracks and pairs coming from primary vertex. The resulting sample of vertices displaced significantly in the radial direction ($\rho > 2.5$ cm) is called the nuclear interactions sample.

In the data 80% of nuclear interactions are reconstructed with 2 tracks and 20% with 3 tracks. In the first case we expect 30% fakes from the simulation, while in the second case the rate of fakes is negligible. Figure 33 shows the map of the nuclear interactions in the x and y coordinates in the region around the beam pipe. The region with more interactions corresponds to the higher density of matter. In this plot the longitudinal coordinate z was restricted to ± 26 cm in order to image well the beam pipe and the first two layers of the central pixel detector. The intensity at which different pixel layers appear is proportional to the convolution of the local particle flux, material density and the track-vertex reconstruction efficiency. Our resolution on the vertex position, roughly 50 μm based on simulation, allows us to produce a sharp picture of the beam pipe and different structures and services of the first pixel layer. One may observe a slight shift of the beam pipe and the first pixel layer with respect to the nominal (0, 0). This shift is not implemented in the simulation used for this analysis.

An alternative view of the material distibution is given by the radial position ρ of the nuclear vertices shown compared to simulation in Fig. 34a. The symmetry over the azimuthal angle enhances the contribution from different pixel structures, allowing us to extend the map up to

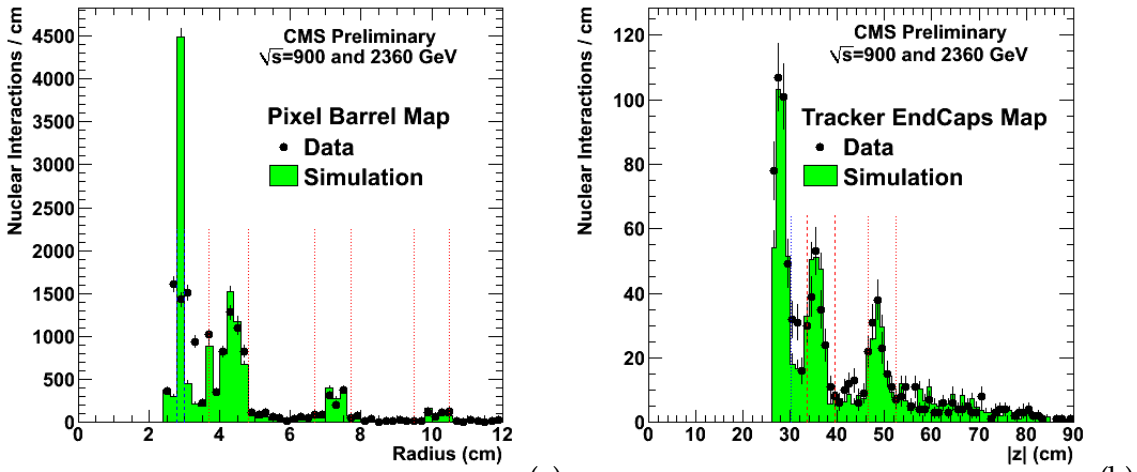

(a) (b)

Figure 34: The nuclear interaction vertices: (a) distribution of the radial position ρ for $|z| < 26$ cm; (b) distribution of the longitudinal coordinate $|z|$ for $|z| > 26$ cm and $\rho < 19$ cm. Black full circles represent the data shown with their statistical uncertainties. The simulation is represented by the green filled histogram. The simulation is normalized to the total number of nuclear interactions found in data in the full z range. Vertical lines represent the limits of the important structures as they are implemented in the CMS detector simulation: red short dashes correspond to sensitive layers, blue long dashes to services.

12 cm where the third pixel barrel layer is located. The ρ variable was corrected in the data for the shift of the first pixel barrel layer in the (x, y) plane. The agreement between the data and the simulation for the relative rate of nuclear interactions in different barrel pixel structures appears to be reasonable. This points toward a consistent description of the material distribution of the pixel tracker implemented in the simulation. In contrast, the beam pipe position in the data appears to be smeared with respect to the simulation. This may be explained by an overall shift of the beam pipe in the (x, y) direction with respect to the first silicon pixel layer.

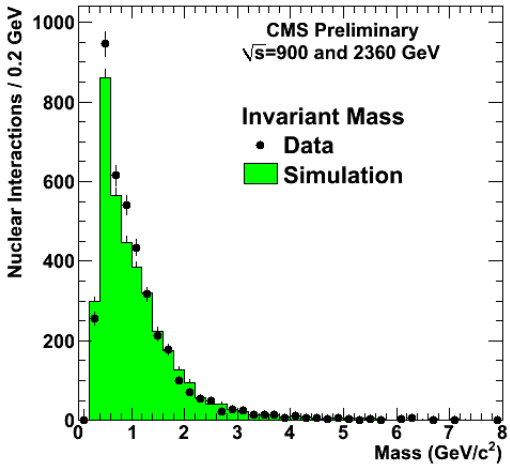

Figure 35: The total invariant mass of the secondary tracks produced in the nuclear interaction. The tracks are treated as pions to compute the invariant mass.

The material distribution in the end cap pixel detector is studied by selecting nuclear interac-

tions with $|z| > 26$ cm and $\rho < 19$ cm. The longitudinal position $|z|$ of the nuclear vertices is shown compared to the Monte Carlo simulation in Fig. 34b. In order to increase the statistical significance of the distribution the forward ($z > 0$ cm) and the backward ($z < 0$ cm) regions are merged together. One can clearly distinguish the pixel barrel flange ($|z| < 30$ cm) and the two pixel disks. The tail at high values of $|z|$ is made of pixel services.

Finally, the invariant mass of the tracks produced in the nuclear interactions is shown in Fig. 35. For the minimum bias events under consideration, the invariant mass spectrum is soft, extending up to 5 GeV/c^2. The non-zero invariant mass of the secondary particles is correlated with some degradation of jet reconstruction.

12 Study of b-tag Related Observables

The measurement of impact parameters and the reconstruction of secondary vertices have been tested on the event sample of December 2009. At higher collision energy these objects will provide the main observables used in b-tagging algorithms [19].

The 2009 data contain only few well-defined jets and mainly tracks at momenta below those typically used in b-tagging. In order to test the reconstruction on a sufficiently large sample a few changes to the recontruction chain have been applied with respect to what is described in [19]. The algorithms are run on tracks associated to anti-k_T particle flow jets [20] with a cone of 0.7 and $p_{\mathrm{T}} > 3\,\mathrm{GeV}$. This allows us to recover low momentum jets made of soft charged tracks. The track selection is also changed in order to accept tracks with $p_{\mathrm{T}} < 1\,\mathrm{GeV}$ and a lower number of hits (7 instead of 8).

The impact parameter is computed with respect to the reconstructed primary vertex and the distributions have been compared between data and a minimum bias simulation reconstructed with the same algorithm settings. The left plot in Figure 36 shows the three dimensional impact parameter significance distribution for all tracks in the jet. The right plot of Figure 36 shows the significance of the signed impact parameter for the so-called *first track above charm*: a fourvector sum is updated by individually adding all the tracks in the jet in decreasing impact parameter significance order (assuming a pion mass). The procedure stops once an invariant mass of at least $m = 1.5\,\mathrm{GeV}$ (slightly below the D^0 meson mass) is reached. The last track added is called *first track above charm*.

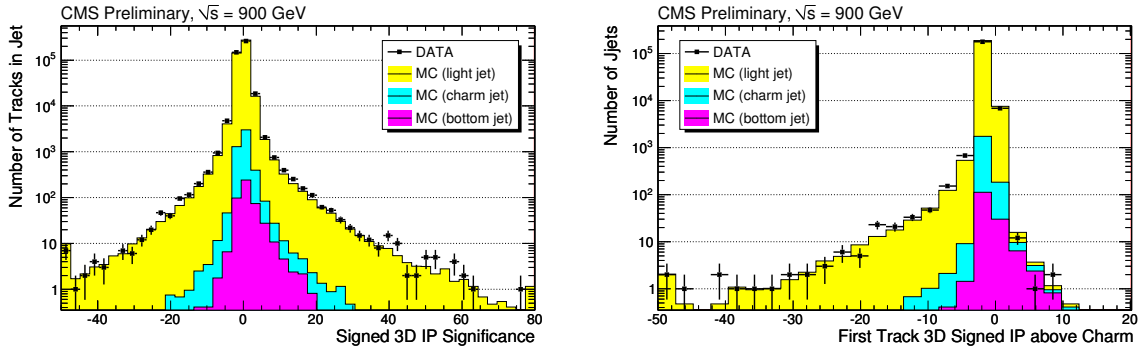

Figure 36: Distribution of the significance of the three-dimensional impact parameter for all tracks in the jet (left) and for the *first track above charm* (right). The data is shown as full circles while the simulated contributions from light flavour, charm and bottom are shown as filled histograms. The two outermost bins contain the respective histogram overflow.

The secondary vertex reconstruction using the tracks associated to jets has been performed with a slightly modified version of algorithm described in [19]. The differences are a looser track selection, a relaxed vertex to jet direction compatibility, the usage of track refitting in the secondary vertex fit, and the usage of the primary vertex constraint rather than the beam spot. In addition, the following K^0_S rejection has been used: $L_{xy} < 2.5\,\text{cm}$ and $|M_{K^0_S} - M_{vtx}| > 0.015\,\text{GeV}/c^2$. The vertex properties have been compared to what is expected from the minimum bias simulation and the results are shown in Figure 37 and 38. All distributions show a good agreement between data and simulation.

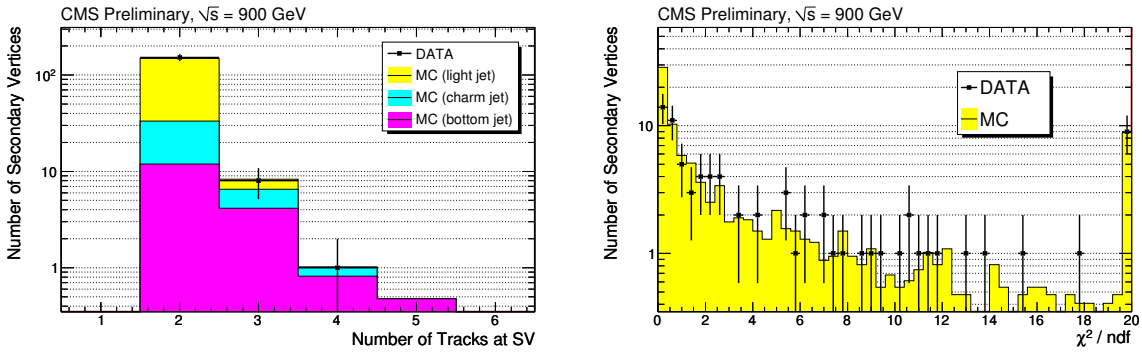

Figure 37: Number of tracks of the secondary vertex (left) and normalized χ^2 for vertices reconstructed inside the jets. The rightmost bins include the histogram overflow.

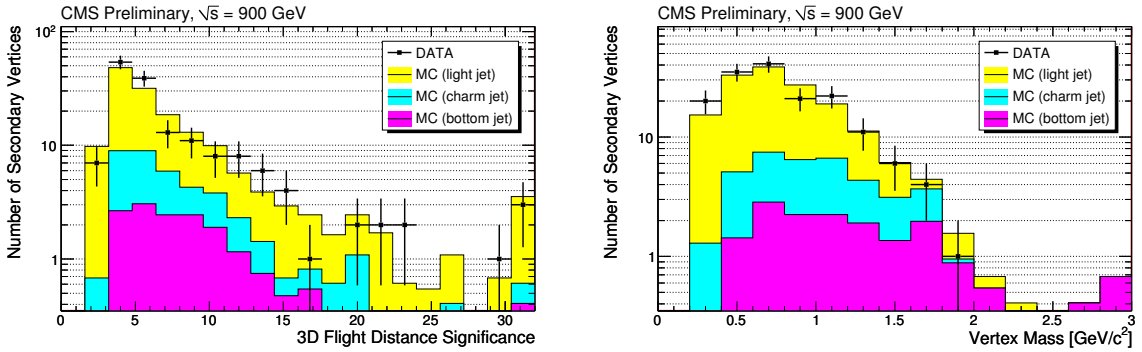

Figure 38: Significance of the vertex 3D decay length (left) and vertex mass (right). The rightmost bins include the histogram overflow.

The secondary vertex reconstruction has also been tested with an inclusive configuration using all tracks in the event. In this case the results near the K^0_S mass have been studied and the results are shown in Figure 39. They demonstrate the sensitivity of the inclusive secondary vertex finder even for two-track vertices.

13 Summary

We have presented the results of studies of reconstructed tracks from the data recorded by CMS at $\sqrt{s} = 900$ GeV and 2.36 TeV in December 2009. The basic kinematic properties of the tracks have been compared with the expectations from simulation. The simulation describes

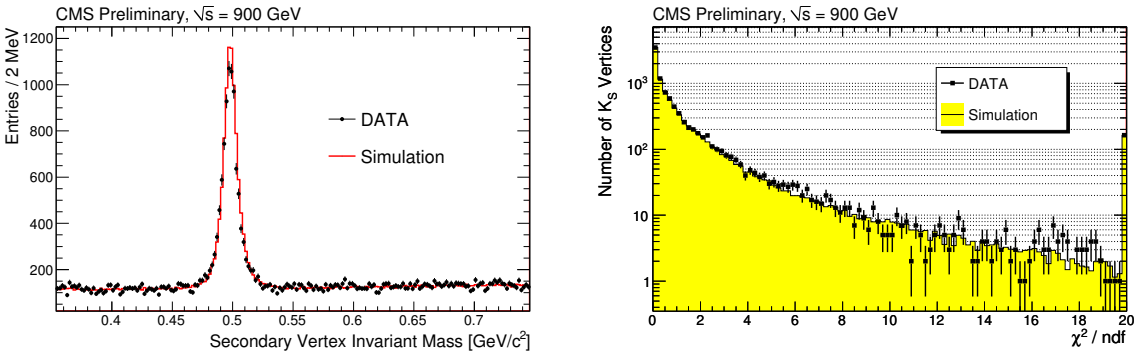

Figure 39: Mass (left) and normalized χ^2 distribution (right) for the inclusive vertex finder in the mass region of $\pm 15\,\text{MeV}$ around the K^0_S resonance. The rightmost bin of the second histogram includes the overflow.

the shape of most of the track properties but not the overall multiplicity or the pseudorapidity. We measured the resolution on the position of the primary interaction vertex and it matches well with the prediction from simulation. We reconstructed clear mass peaks in the decays of of K^0_S, Λ, ϕ, $\Xi^{\pm}$, and $K^{\star}(892)^{\pm}$. The fitted masses are all in agreement with the PDG values. The reconstruction of $\phi \to K^+K^-$ demonstrates the application of dE/dx for particle ID. For the K^0_S and Λ, we measured the lifetimes and obtained values in agreement with the PDG values. We reconstructed both photon conversions and nuclear interactions as a first investigation of the tracker material. Finally, we studied the basic observables used in b-tagging and found good agreement with simulation.

References

[1] W. Adam, B. Mangano, T. Speer et al., "Track Reconstruction in the CMS Tracker", *CMS Note* **2006/041** (2006).

[2] **CMS** Collaboration, "Transverse momentum and pseudorapidity distributions of charged hadrons in pp collisions at sqrt(s) = 0.9 and 2.36 TeV", *JHEP* **02** (2010) 041. doi:10.1007/JHEP02(2010)041.

[3] **CMS** Collaboration, S. Chatrchyan et al., "Alignment of the CMS Silicon Tracker during Commissioning with Cosmic Rays", arXiv:0910.2505.

[4] T. Sjöstrand et al., "PYTHIA 6.4 Physics and Manual", *JHEP* **05** (2006) 026.

[5] P. Bartalini, (ed.) and L. Fano', (ed.), "Proceedings of the 1st Workshop: Multiple Parton Interactions at the LHC, Perugia, Italy, October 27-31, 2008", **DESY-PROC-2009-06** (2009).

[6] J. Allison et al., "Geant4 developments and applications", *IEEE Transaction on Nuclear Science* **53 No.1** (2006) 270.

[7] R. Fruewirth, W. Waltenberger, and P. Vanlaer, "Adaptive Vertex Fitting", *CMS Note* **2007/008** (2007).

[8] T. Miao, H. Wenzel, and F. Yumiceva, "Beam Position Determination Using Tracks", *CMS Note* **2007/021** (2007).

[9] C. Amsler et al., "Review of Particle Physics", *Physics Letters* **B667** (2008) 1.

[10] **CDF** Collaboration, D. E. Acosta et al., "K^0_S and Λ^0 production studies in $p\bar{p}$ collisions at $\sqrt{s} = 1800$-GeV and 630-GeV", *Phys. Rev.* **D72** (2005) 052001. doi:10.1103/PhysRevD.72.052001.

[11] The CMS Collaboration, "Search for Heavy Stable Charged Particles with 100 pb^{-1} and 1 fb^{-1} in the CMS experiment", *CMS Physics Analysis Summary* **EXO-08-003** (2008).

[12] A. Giammanco, "Particle Identification with Energy Loss in the CMS Silicon Strip Tracker", *CMS Note* **2008/005** (2008).

[13] The CMS Collaboration, "Commissioning and Performance of the CMS Silicon Strip Tracker with Cosmic Ray Muons", *CMS Physics Analysis Summary* **CFT-09-002** (2009).

[14] R. Armenteros et al., "The Properties of Charged V Particles", *Phil. Mag.* **42** (1951).

[15] D. E. Groom et al., "Review of Particle Physics", *The European Physical Journal* **C 15** (2001) 1.

[16] N. Marinelli, "Track finding and identification of converted photons", *CMS Note* **2006/005** (2006).

[17] J. Marriner, "Secondary vertex fit with mass and pointing constraints (CTVMFT)", *CDF Note* **1996** (1993).

[18] R. Ranieri, "The Simulation of the CMS Silicon Tracker", *CMS Conference Report* **2008/007** (2007).

[19] CMS Collaboration, "Algorithms for b Jet identification in CMS", *CMS Physics Analysis Summary* **BTV-09-001** (2009).

[20] CMS Collaboration, "Jets in 0.9 and 2.36 TeV pp Collisions", *CMS Physics Analysis Summary* **JME-10-001** (2009).

A Selection of highPurity Tracks

At the end of each iteration in track reconstruction, tracks are filtered to remove those that are likely fakes. Many of the fake tracks can be removed by selecting tracks that have a good fit χ^2 and are compatible with the beamline or the primary vertices of the event. This selection can be refined further by varying the cuts for the track p_{T} , η, and the number of layers with hits. Short tracks with few hits are far more likely to be fakes, so a tighter selection should be applied. In contrast, tracks with hits on every layer are unlikely to be fakes and a much looser selection can be used.

We select tracks based on eight quantities:

- track normalized χ^2
- transverse impact parameter d_{xy} with respect to the beamspot
- longitudinal impact parameter d_z with respect to the closest HLT primary vertex
- significance of the transverse impact parameter $d_{xy}/\delta_{d_{xy}}$, where $\delta_{d_{xy}}$ is the uncertainty on d_{xy} from the track fit
- significance of the longitudinal impact parameter d_z/δ_{d_z}, where δ_{d_z} is the uncertainty on d_z from the track fit
- number of tracker layers with a hit on the track, n_{layers}
- number of tracker "3D" layers with a hit on the track (either pixel layers or matched strip layers), $n_{\text{3D layers}}$
- number of layers missing hits between the first and last hit on the track, $n_{\text{lost layers}}$

Resolutions on d_{xy} and d_z are parameterized as $\sigma_{d_{xy}} = \sqrt{a^2 + (b/p_{\mathrm{T}})^2}$ and $\sigma_{d_z} = \cosh(\eta) \cdot \sigma_{d_{xy}}$. For highPurity tracks, $a = 30$ μm and $b = 10$ μm$\cdot$ GeV/c. Selection cuts were optimized on simulated data samples, considering processes of varying multiplicity, leading to the following formulas used for the selection on the first five quantities in the previous list:

- Normalized $\chi^2 < \alpha_0 \cdot n_{\text{layers}}$
- $|d_{xy}| < (\alpha_1 \cdot n_{\text{layers}})^{\beta} \cdot \sigma_{d_{xy}}$
- $|d_z| < (\alpha_2 \cdot n_{\text{layers}})^{\beta} \cdot \sigma_{d_z}$
- $d_{xy}/\delta_{d_{xy}} < (\alpha_3 \cdot n_{\text{layers}})^{\beta}$
- $d_z/\delta_{d_z} < (\alpha_4 \cdot n_{\text{layers}})^{\beta}$

The values of α_i and β are configurable and different values are used for each tracking iteration. The values for all the parameters used in track selection are listed in Table 5.

B Armenteros plots

One way to view two-body decays of neutral particles is through the use of an Armenteros plot [14]. In this plot, the y-axis shows the transverse momentum of the positive decay track relative to the neutral parent particle momentum direction. The x-axis shows the asymmetry of the longitudinal momentum of the two charged particles along the neutral parent particle momentum direction. The Armenteros plot shown in Fig. 40 is obtained from V^0 candidates reconstructed as described in Section 7.1. There is no mass cut on these candidates. The K^0_S signal is visible as a single curve extending up to 0.2 GeV/c on the y-axis. The Λ^0 ($\overline{\Lambda}^0$) signal is seen as a small curve on the right (left) side of the plot.

Table 5: Parameter values used for selection of highPurity tracks in each tracking iteration. Note that in iterations 2 and 3, there are two separate sets of cuts applied, where one focuses on track quality (2_{TRK}, 3_{TRK}) and the other focuses on vertex compatibility (2_{VTX}, 3_{VTX}).

Iteration	n^{min}_{layers}	$n^{min}_{\text{3D layers}}$	$n^{max}_{\text{lost layers}}$	β	α_0	α_1	α_2	α_3	α_4
0	4	4	2	4	0.90	0.30	0.35	0.40	0.40
1	4	4	2	4	0.90	0.30	0.35	0.40	0.40
2_{TRK}	5	3	1	4	0.50	0.90	0.90	0.90	0.90
2_{VTX}	3	3	1	3	0.90	0.85	0.80	0.90	0.90
3_{TRK}	5	4	1	4	0.50	1.00	1.00	1.00	1.00
3_{VTX}	3	3	1	3	0.90	0.90	0.90	1.00	1.00
4	6	3	0	4	0.30	1.00	1.00	1.00	1.00
5	6	2	0	4	0.25	1.20	1.10	1.20	1.10

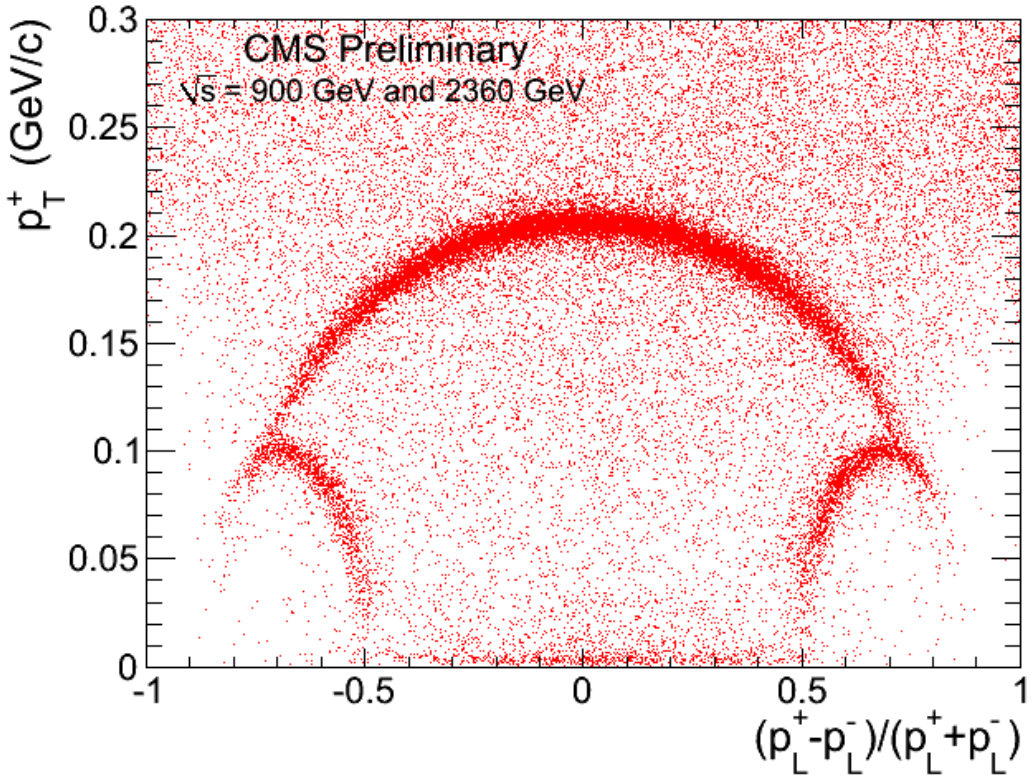

Figure 40: Armenteros plot for V^0 candidates.

C Event display of a candidate Ξ^+ decay

A display of an event containing a Ξ^+ candidate is shown in Fig. 41 with the description given in the caption.

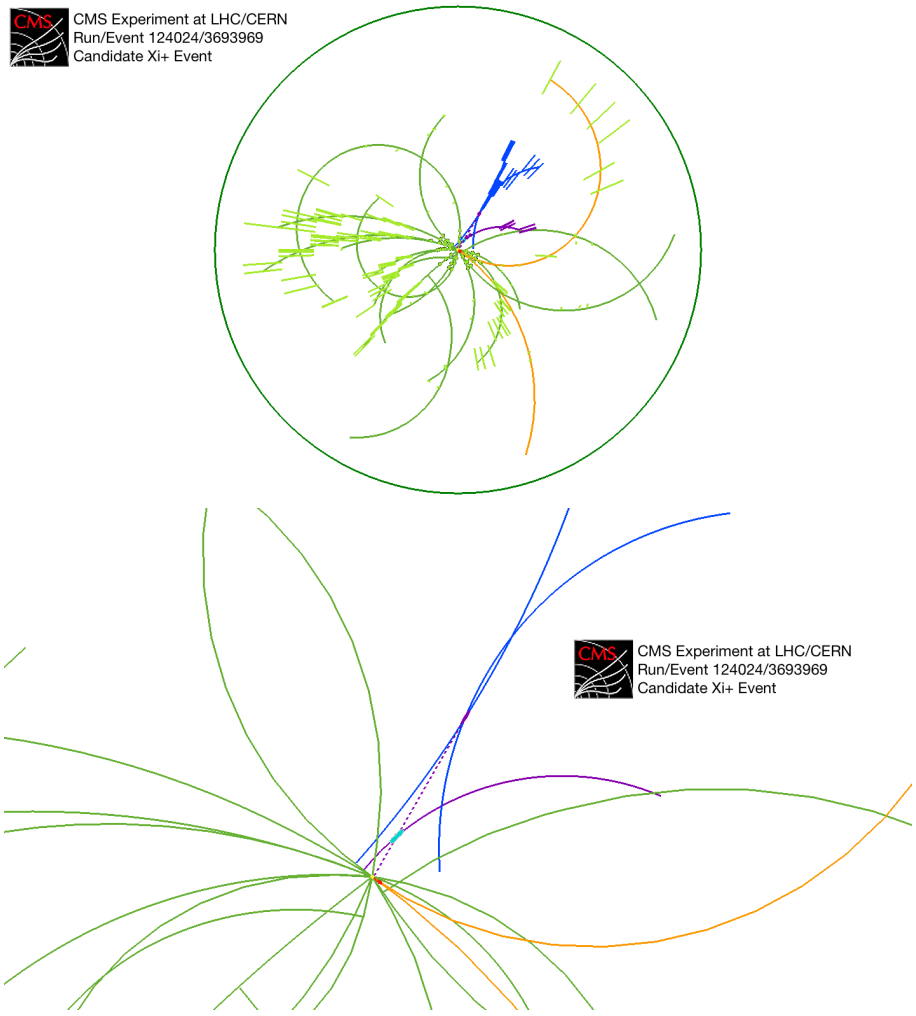

Figure 41: Event display for an event with a Ξ^+ decaying to a $\overline{\Lambda}^0\pi^+$. The Ξ^+ decay vertex is shown in cyan. The π^+ from the Ξ^+ decay is shown in purple. The $\overline{\Lambda}^0$ momentum vector is shown as a dashed purple line. The $\overline{\Lambda}^0$ decays to $\overline{p}\pi^+$ at the purple ellipse and the decay products are shown as blue curves. A candidate K^0_S is also reconstructed close to the primary and shown by the red vertex decaying into two orange tracks. Both plots show the $r-\phi$ view. The top plot shows the entire tracker with the tracker hits shown while the bottom plot is zoomed in to the region of interest and without tracker hits.